The Astrophysical Journal, 890:129 (18pp), 2020 February 20 https://doi.org/10.3847/1538-4357/ab659e

Detection of Irregular, Submillimeter Opaque Structures in the Orion Molecular Clouds: Protostars within 10,000 yr of Formation?

N. Karnath[1,11], S. T. Megeath[1], J. J. Tobin[2], A. Stutz[3,4], Z.-Y. Li[5], P. Sheehan[2], N. Reynolds[6], S. Sadavoy[7], I. W. Stephens[8], M. Osorio[9], G. Anglada[9], A. K. Díaz-Rodríguez[9], and E. Cox[10]
[1] Ritter Astrophysical Research Center, University of Toledo, 2801 W. Bancroft Street, Toledo, OH 43606, USA; nkarnath@sofia.usra.edu
[2] National Radio Astronomy Observatory, 520 Edgemont Road, Charlottesville, VA 22903-2475, USA
[3] Departmento de Astronomía, Facultad de Ciencias Físicas y Matemáticas, Universidad de Concepción, Concepción, Chile
[4] Max-Planck-Institute for Astronomy, Königstuhl 17, D-69117 Heidelberg, Germany
[5] Department of Astronomy, University of Virginia, Charlottesville, VA 22903, USA
[6] Homer L. Dodge Department of Physics and Astronomy, University of Oklahoma, 440 W. Brooks Street, Norman, OK 73019, USA
[7] Department of Physics, Engineering Physics, and Astronomy, Queen's University, Kingston, ON K7L 3N6, Canada
[8] Harvard-Smithsonian Center for Astrophysics, 60 Garden Street, Cambridge, MA, USA
[9] Instituto de Astrofísica de Andalucía, CSIC, Glorieta de la Astronomía, s/n, E-18008 Granada, Spain
[10] Center for Interdisciplinary Exploration and Research in Astrophysics (CIERA), Department of Physics & Astronomy, Northwestern University, 2145 N. Sheridan Road, Evanston, IL 60208, USA
Received 2019 October 2; revised 2019 December 12; accepted 2019 December 23; published 2020 February 20

Abstract

We report Atacama Large Millimeter/submillimeter Array and Very Large Array continuum observations that potentially identify the four youngest protostars in the Orion Molecular Clouds taken as part of the Orion VANDAM program. These are distinguished by bright, extended, irregular emission at 0.87 and 8 mm and are optically thick at 0.87 mm. These structures are distinct from the disk or point-like morphologies seen toward the other Orion protostars. The 0.87 mm emission implies temperatures of 41–170 K, requiring internal heating. The bright 8 mm emission implies masses of 0.5–1.2 $M_{\odot}$ assuming standard dust opacity models. One source has a Class 0 companion, while another exhibits substructure indicating a companion candidate. Three compact outflows are detected, two of which may be driven by companions, with dynamical times of ∼300 to ∼1400 yr. The slowest outflow may be driven by a first hydrostatic core. These protostars appear to trace an early phase when the centers of collapsing fragments become optically thick to their own radiation and compression raises the gas temperature. This phase is thought to accompany the formation of hydrostatic cores. A key question is whether these structures are evolving on freefall times of ∼100 yr, or whether they are evolving on Kelvin–Helmholtz times of several thousand years. The number of these sources imply a lifetime of ∼6000 yr, in closer agreement with the Kelvin–Helmholtz time. In this case, rotational and/or magnetic support could be slowing the collapse.

Unified Astronomy Thesaurus concepts: Protostars (1302); Star formation (1569); Stellar jets (1607)

1. Introduction

The transition from a dense collapsing clump of gas and dust in a fragmenting cloud to an accreting protostar is perhaps the most challenging phase of a star's birth to observe. This transition occurs within the dense centers of these collapsing objects, where increases in temperature and pressure slow collapse and ultimately lead to the formation of opaque hydrostatically supported cores (hereafter HSCs[12]). Theoretical studies have linked this transition to high optical depth. Early studies on opacity-limited star formation produced models that predicted hierarchical Jeans fragmentation of clouds would cease when the fragments became optically thick to their own radiation (Low & Lynden-Bell 1976; Rees 1976; Silk 1977). Numerical simulations following the collapse of spherical, constant density fragments showed that the formation of an optically thick region precedes the formation of HSCs (e.g., Larson 1969). In these studies (e.g., Masunaga et al. 1998), the initial, isothermal collapse was characterized by a contracting, constant density, central region with a diameter approximately equal to the Jeans length surrounded by a $\rho \propto r^{-2}$ envelope. Masunaga et al. (1998) argued that an HSC forms when heating by compression in the limit of constant density exceeds cooling by radiation. They found that this transition occurs at approximately 10^{-13} g cm^{-3}, the density at which the core becomes optically thick to its own radiation.

Numerical simulations of this transition have been ongoing for decades, including by Larson (1969), Masunaga et al. (1998), Masunaga & Inutsuka (2000), Commerçon et al. (2011), Vaytet et al. (2013), Bate et al. (2014), Bhandare et al. (2018), and others. Larson (1969) was the first numerical study to show that an increase in temperature and pressure led to the formation of a very low-mass, first hydrostatic core (hereafter FHSC), comprised of molecular hydrogen. As the accreting FHSC grows in mass and the central temperature reaches ∼2000 K, the dissociation of the H_2 molecules causes the FHSC to collapse and form the second hydrostatic core. The appearance of the second HSC is expected to mark the onset of the Class 0 protostar phase, and the central, hydrostatically supported protostar will continue to grow in mass as it accretes from the infalling envelope and disk. The work of Larson (1969) assumed initial conditions of spherical symmetry, constant density, and no rotation, turbulence, or magnetic fields. Since Larson's work, many contributions have shown that magnetic fields (Basu & Mouschovias 1994; Tomisaka 2002; Commerçon et al. 2011)

[11] Current Address: SOFIA Science Center, USRA, NASA Ames Research Center, Moffett Field, CA 94035, USA.
[12] We refer to the dense, isothermal regions of clouds undergoing collapse as fragments and the hydrostatically supported objects in the centers of the fragments as cores. In the literature, the phrase "molecular core" is often used to describe what we refer to as fragments, e.g., Bergin & Tafalla (2007).

and rotation (Tsuribe & Inutsuka 1999a, 1999b) can influence collapse and lead to the formation of disks or disk-like structures and outflows during the FHSC phase, i.e., before the formation of the protostar (e.g., Saigo et al. 2000; Matsumoto & Hanawa 2003; Bate et al. 2014).

Observations of this transition are challenging due to the high optical depths at the centers of the fragment, i.e., the opaque regions where the HSCs form, the small spatial extent of the nascent HSCs, and their rapid evolution. With the sensitivity and resolution of submillimeter/millimeter interferometers such as Atacama Large Millimeter/submillimeter Array (ALMA) and the Very Large Array (VLA), however, we can now detect and resolve the dense, opaque regions of collapsing fragments. The observations presented in this paper improve our understanding of star formation in a regime that has been previously restricted to theoretical investigations. A couple of opaque core candidates have been found in the literature thus far, for example, Cox et al. (2015) and Hernández-Gómez et al. (2019); these demonstrate the need for long-wavelength observations with ALMA and VLA to detect such deeply embedded objects.

Given the rapid evolution of this transitional phase, surveys of hundreds of protostars are required to detect even a few examples. The VLA/ALMA Nascent Disk and Multiplicity (VANDAM) survey in Orion (Tobin et al. 2020) observed 328 *Herschel* Orion Protostellar Survey (HOPS; Fischer et al. 2013; Furlan et al. 2016) protostars with ALMA at 0.87 mm and 148 protostars with VLA at 8 mm and 1 cm with ∼40 au spatial resolution. These include 19 extremely red (70 μm) protostars, or "PACS Bright Red Sources" (hereafter PBRs; Stutz et al. 2013). Using imaging from the *Spitzer Space Telescope* and the *Herschel Space Observatory*, Stutz et al. (2013) identified this sample of 18 protostars; one additional PBR has been identified since (Tobin et al. 2015). They are distinguished by their weak mid-IR emission and red 70–24 μm colors; 11 of the PBRs were not identified as protostars by *Spitzer* due to their faint 24 μm fluxes, and eight were not detected by *Spitzer* at $\lambda \leqslant 24$ μm. Subsequent CARMA observations showed the PBRs had high $L_{2.9\,\mathrm{mm}}/L_{\mathrm{bol}}$ ratios compared to other Class 0 protostars (Tobin et al. 2015). Using radiative transfer models to demonstrate the PBRs were internally heated, Stutz et al. (2013) interpreted the PBRs as very young Class 0 protostars. The red colors and rarity of PBRs suggest that they represent an early phase of protostellar evolution with a duration of ∼10,000 yr (Stutz et al. 2013).

We present here the detection of four previously identified PBRs (HOPS 400-B, HOPS 402, HOPS 403, and HOPS 404) that show extended, irregular morphologies in VLA (8 mm) and ALMA (0.87 mm) imaging unlike the vast majority of the VANDAM protostar sample. These irregular PBRs are of particular interest because of their large and asymmetric structures. Two additional protostars are discussed to a smaller extent, a Class 0 protostellar companion to an extended PBR (HOPS 400-A) and a more compact PBR in spatial proximity to an extended PBR (HOPS 401). All of the PBRs presented here are found in Orion B, and we adopt a common distance of 400 pc for all protostars in this study (Kounkel et al. 2018). We find that the inner, ∼160 au regions resolved by ALMA and the VLA are optically thick at 0.87 mm, indicating that they may be the theoretically predicted, opaque regions at the earliest stages of HSC formation. Using the masses, luminosities, and number of the optically thick regions, as well as detections of outflows in ^{12}CO, we assess the timescales of these protostars and compare their properties to those anticipated by simulations. We find that these observations challenge current models that predict small (a few astronomical units) optically thick regions and thermally supported cores. We discuss possible solutions for resolving these challenges.

The paper is organized as follows: in Section 2, we describe the observations and reduction of the data presented, Section 3 contains the observational results, Section 4 presents the discussion and possible scenarios for varying collapse timescales and support mechanisms, the summary is in Section 5, and the Appendix contains the details of each source.

2. Observations and Data Reduction

2.1. ALMA 0.87 mm Observations and Reduction

The Cycle 4 ALMA 0.87 mm observations were conducted on 2016 September 4 and 5, and 2017 July 19 for which 34, 39, and 42 antennas were operating, respectively, with baselines between 15.1 and 3697 m. The total time spent on each target was ∼0.9 minutes.

The correlator was configured with two basebands set to 1.875 GHz bandwidth, centered at 333 and 344 GHz. One of the remaining basebands was centered on ^{12}CO ($J = 3 \rightarrow 2$) at 345.79599 GHz with a total bandwidth of 937.5 MHz and 0.489 km s^{-1} channels. The last remaining baseband was centered on ^{13}CO ($J = 3 \rightarrow 2$) at 330.58797 GHz, with a bandwidth of 234.375 MHz and 0.128 km s^{-1} channels. The line-free-regions of the basebands were used for additional continuum bandwidth. The total aggregate continuum bandwidth was ∼4.75 GHz.

The data were manually reduced and imaged using the Common Astronomy Software Application (CASA; McMullin et al. 2007) by the Dutch Allegro ARC Node. We used CASA 4.7.2 for all self-calibration and imaging. Following the standard calibration, up to three rounds of phase-only self-calibration were performed on the continuum data to increase the signal-to-noise ratio. The self-calibration solutions were also applied to the spectral line data. Final continuum and spectral line data cubes were then produced.

The continuum images were deconvolved using Briggs weighting with a robust parameter of 0.5, yielding a synthesized beam of $0\farcs11 \times 0\farcs10$ (44 au × 40 au). The continuum images also only use *uv* points at baselines >25 $k\lambda$ to mitigate striping resulting from large-scale emission that is not properly recovered. The spectral line data were deconvolved using natural weighting for baselines >50 $k\lambda$ with an outer taper of 500 $k\lambda$ applied to increase the sensitivity to extended structure, yielding synthesized beams of $0\farcs25 \times 0\farcs24$. The continuum subtraction was done using line-free regions of the spectral windows to estimate the continuum level using the uvcontsub task. The resulting rms noise of the continuum images, ^{12}CO data cubes, and ^{13}CO data cubes are ∼0.31 mJy beam^{-1}, 17.7 mJy beam^{-1} (1 km s^{-1} channels), and 33.3 mJy beam^{-1} (0.44 km s^{-1} channels), respectively. The flux density of the objects and surrounding extended structure are measured both using Gaussian fitting and a measurement within a polygon region; these yield measured flux densities that are within the uncertainty of one another. For consistency with Tobin et al. (2020), we use the Gaussian fitting results in our tables and analysis. The peak and integrated flux densities with uncertainties and the positions are given in Table 1. The absolute flux calibration accuracy is

Table 1
Observed Properties of Sources

HOPS ID	Type of PBR	Centroid Positions		VLA (8.1 mm)		ALMA (0.87 mm)	
		R.A.[a] (J2000)	Decl.[a] (J2000)	Flux Density (mJy)	Intensity Peak (mJy/beam)	Flux Density[b] (mJy)	Intensity Peak[b] (mJy/beam)
400-A	regular	05:42:45.25	−01:16:13.64	0.802 ± 0.020	0.524 ± 0.008	147.7 ± 7.3	67.9 ± 2.0
400-B	irregular	05:42:45.26	−01:16:14.14	2.598 ± 0.088	0.254 ± 0.008	657.1 ± 19.3	49.4 ± 2.0
401	regular	05:46:07.65	−00:12:20.73	0.328 ± 0.028	0.146 ± 0.007	128.9 ± 2.9	40.1 ± 0.6
402	irregular	05:46:09.97	−00:12:16.85	2.117 ± 0.093	0.149 ± 0.008	419.4 ± 9.8	35.5 ± 1.1
403	irregular	05:46:27.75	−00:00:53.81	3.803 ± 0.105	0.295 ± 0.008	584.1 ± 12.8	41.6 ± 1.3
404	irregular	05:48:07.76	00:33:50.79	3.333 ± 0.059	0.697 ± 0.011	306.4 ± 6.2	99.5 ± 1.5

Notes.
[a] The positions are based on the VLA maps of the peak emission at 8 mm.
[b] The reported uncertainties are statistical uncertainties and do not include the calibration error of ∼10% in both VLA and ALMA.

expected to be ∼10%, and comparisons of the observed flux densities for the science targets for different executions are consistent with this level of accuracy. The uncertainties in Table 1 are the statistical uncertainties and do not include the calibration error.

2.2. VLA Observations and Reduction

The observations with the VLA were conducted in the A-configuration on 2016 October 21, 23, 29, and 31 and December 19. Each target typically was observed individually in a single execution with ∼1 hr on target. The observations used the *Ka*-band receivers, and the correlator was used in the wide bandwidth mode (3 bit samplers) with one 4 GHz baseband centered at 36.9 GHz (8.1 mm) and the second 4 GHz baseband centered at 29 GHz (1.03 cm). We chose to use the 8.1 mm data over the combination of 8.1 mm and 1 cm data to maximize the dust emission over a smaller bandwidth; the 8.1 mm data has higher flux densities than 1 cm, which is better for studying the dust emission.

The data were reduced using the scripted version of the VLA pipeline in CASA 4.4.0. The continuum was imaged using the clean task in CASA 4.5.1 using natural weighting, multi-frequency synthesis with *n*terms = 1 across both basebands. The synthesized beams are $0\farcs08 \times 0\farcs07$ (32 au × 28 au).

The flux density of the objects and surrounding extended structure is measured using both Gaussian fitting and by integrating the intensity over a polygonal region; just as found for the ALMA data, these two approaches yield results that are within the uncertainties of one another. Using the Gaussian value, the peak and integrated flux densities with statistical uncertainties and the positions are given in Table 1. The absolute flux calibration accuracy of the VLA is expected to be ∼10%. The uncertainties in Table 1 are the statistical uncertainties and do not include the calibration error.

3. Results

Although all 19 currently known PBRs were observed by the VLA and ALMA, we focus primarily on the four with bright emission at 8 mm and extended, irregular-shaped morphologies in both wavelengths: HOPS 400-B, 402, 403, and 404 (Furlan et al. 2016). These four PBRs are unique among not only the PBR sample but the entire VANDAM sample: their large and asymmetric structures set these sources apart. Two nearby protostars are also included in this analysis: HOPS 400-A, which is a PBR and a Class 0 companion to the irregular PBR; HOPS 400-B; and HOPS 401, which is a very red PBR. HOPS 401 appears to be a more compact, potentially irregular source and is found within 15,000 au of the irregular PBR, HOPS 402. We tabulate and display the properties of HOPS 400-A and HOPS 401 in this section, but we defer discussion of those sources to Section 4 and the Appendix.

3.1. Flux Densities and Morphologies

Figure 1 shows the 0.87 and 8 mm flux densities, via Gaussian fits for consistency, for the entire PBR sample of Stutz et al. (2013) and Tobin et al. (2015). The four irregular PBRs that are the focus of this paper, HOPS 400-B, 402, 403, and 404, are located on the upper right. Their 0.87 mm flux densities are among the highest of the sample and their 8 mm flux densities exceed those of all the PBRs. The four irregulars in our sample have a spectral index of 2–3 between 0.87 mm and 8 mm, indicating thermal dust emission. In contrast, HOPS 354 has a spectral index lower than 2, suggesting that there is significant free–free emission in this source. The four irregular PBRs in the upper right of Figure 1 are also above the median 2.9 mm flux density of the PBRs (Tobin et al. 2015). This is consistent with the ALMA and VLA flux densities being dominated by strong thermal dust emission and supports the interpretation that the irregular PBRs have the most massive, densest inner envelopes of the 19 PBRs.

The bolometric luminosity and temperature (BLT) diagram for the PBRs is also presented in Figure 1. The $L_{\rm bol}$ and $T_{\rm bol}$ values of the four irregular protostars are consistent with the other PBRs (see also Stutz et al. 2013, Figure 14). Two of the irregular protostars, HOPS 402 and HOPS 404, and the protostar HOPS 401 have relatively low values for $T_{\rm bol}$ and $L_{\rm bol}$ compared to all HOPS Class 0 protostars (Fischer et al. 2017). As described later, the presence of more evolved companions that are unresolved in the IR data may explain the higher values of $T_{\rm bol}$ and $L_{\rm bol}$ for HOPS 400 and perhaps also for HOPS 403.

The continuum images of the PBR sample studied in this paper are shown in Figure 2. See the Appendix for more details on each source. HOPS 400 is a resolved binary, and we refer to the northern, compact Class 0 PBR as 400-A and the southern, extended, irregular companion as 400-B. HOPS 402 is asymmetric in both 0.87 and 8 mm images with no point-like peak resolved at 8 mm. HOPS 403 shows a point-like peak at 8 mm that is coincident with the more elongated, lower contrast 0.87 mm peak, and a second weaker peak at 8 mm. We classify HOPS 404 as an irregular because it shows a square shape

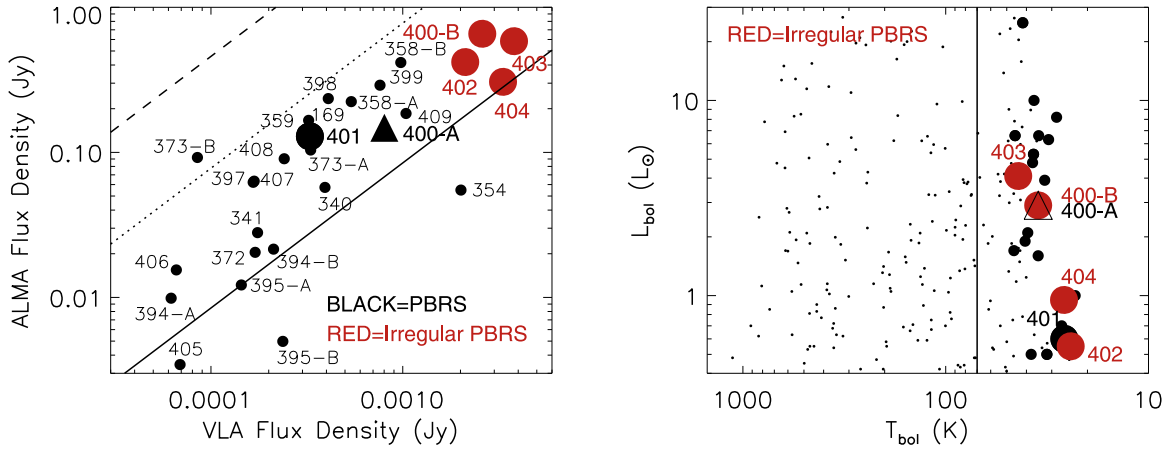

Figure 1. Left: ALMA flux density vs. VLA flux density for the PBRs in the VANDAM Orion survey. The large red points are the four irregular PBRs; HOPS 401 and HOPS 400-A are the large black point and triangle, respectively. The smaller black points are the remaining PBR samples. The overlaid lines are spectral indices between 8 mm and 0.87 mm of 2 (solid), 3 (dotted), and 3.8 (dashed). The four opaque irregular PBRs are bright at both wavelengths making them stick out from the rest of the sample. Right: L_{bol} vs. T_{bol} for the irregular PBRs (red) plus HOPS 401 and HOPS 400-A as the large black point and triangle, respectively. The medium-sized black points are the remaining PBR samples, and the small black points are the entire Orion VANDAM sample (Class 0 to Flat Spectrum protostars). The vertical line at 70 K delimits the Class 0 sources from the Class I sources (e.g., Furlan et al. 2016). The irregular PBRs fit into the rest of the PBR sample and do not stick out in L_{bol} vs. T_{bol} space, aside from having among the lowest T_{bol}.

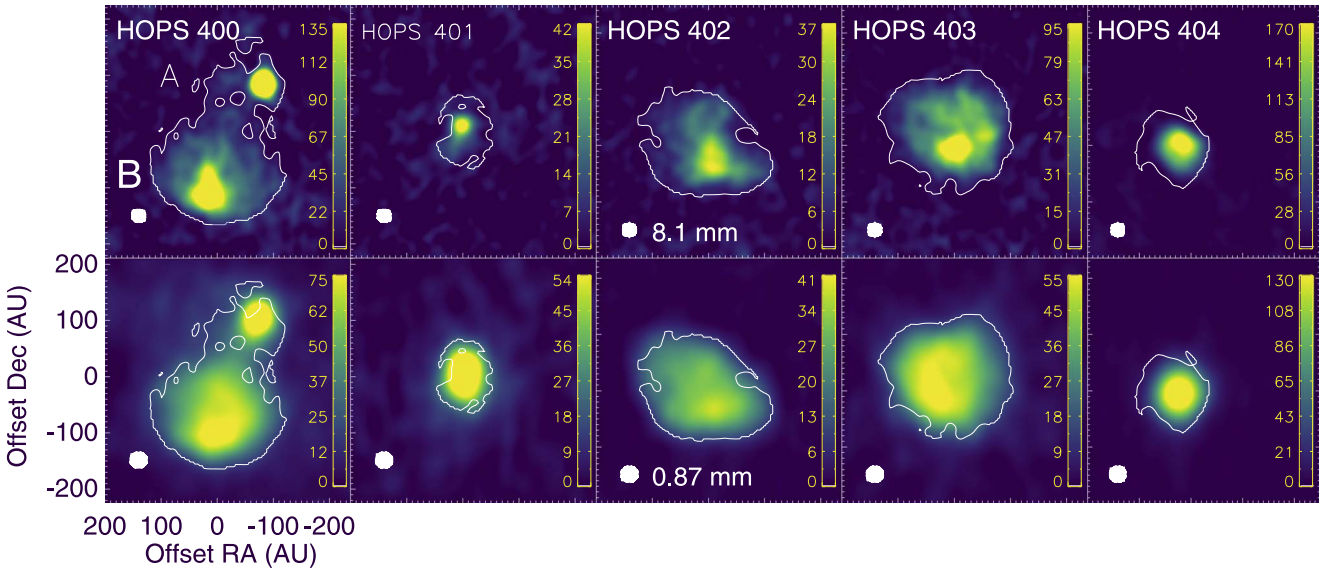

Figure 2. Continuum images with VLA (8.1 mm, top) and ALMA (at 0.87 mm, bottom) of HOPS 400-404. HOPS 401 is discussed in the Appendix. The color bars represent the brightness temperature scales in each individual panel. The contours represent where $\tau = 1$ (see Equation (1)) for the 0.87 mm continuum emission assuming $\beta = 1$. The coordinates are oriented with R.A.–decl. (J2000) at a distance of 400 pc. The synthesized beams are overlaid in the bottom-left corners of the image, FWHM = 42 au in ALMA and 30 au in VLA.

with an offset peak at 8 mm, although it has more circular morphology at 0.87 mm. Overall, the four irregular PBRs are more extended and show more highly structured emission in the 0.87 mm images than the rest of the VANDAM sample (Tobin et al. 2020). The extended, irregular emission at 0.87 and 8 mm separates them from the remainder of the PBRs and other Class 0 protostars (Tobin et al. 2020).

3.2. Brightness Temperature Profiles

Assuming the emission lies within the Rayleigh–Jeans limit, Figure 3 plots the brightness temperature profile cuts at 0.87 mm and 8 mm along R.A. and are centered on the 8 mm peaks. Given a constant dust temperature, the ratio of the brightness temperatures is given by the equation:

$$\frac{T_b(8\text{ mm})}{T_b(0.87\text{ mm})} = \frac{1 - e^{-\tau_{0.87}\left(\frac{0.87\text{ mm}}{8\text{ mm}}\right)^{\beta}}}{1 - e^{-\tau_{0.87}}}, \quad (1)$$

where τ_{870} is the optical depth at 0.87 mm and β is the dust opacity index. For β ranging from 1.8 to 1, which is typical in protostellar envelopes (Ossenkopf & Henning 1994; Ormel et al. 2011), the expected brightness temperature ratios should be between ~0.01 and ~0.1. When the ratio of the 8 mm to 0.87 mm brightness temperature exceeds 0.16 assuming $\beta = 1$ (or exceeds 0.03 with $\beta = 1.8$), the 0.87 mm emission becomes optically thick ($\tau > 1$). In Figure 3, vertical lines indicate where $\tau_{0.87\text{ mm}}$ exceeds 1, and the 0.87 mm emission becomes

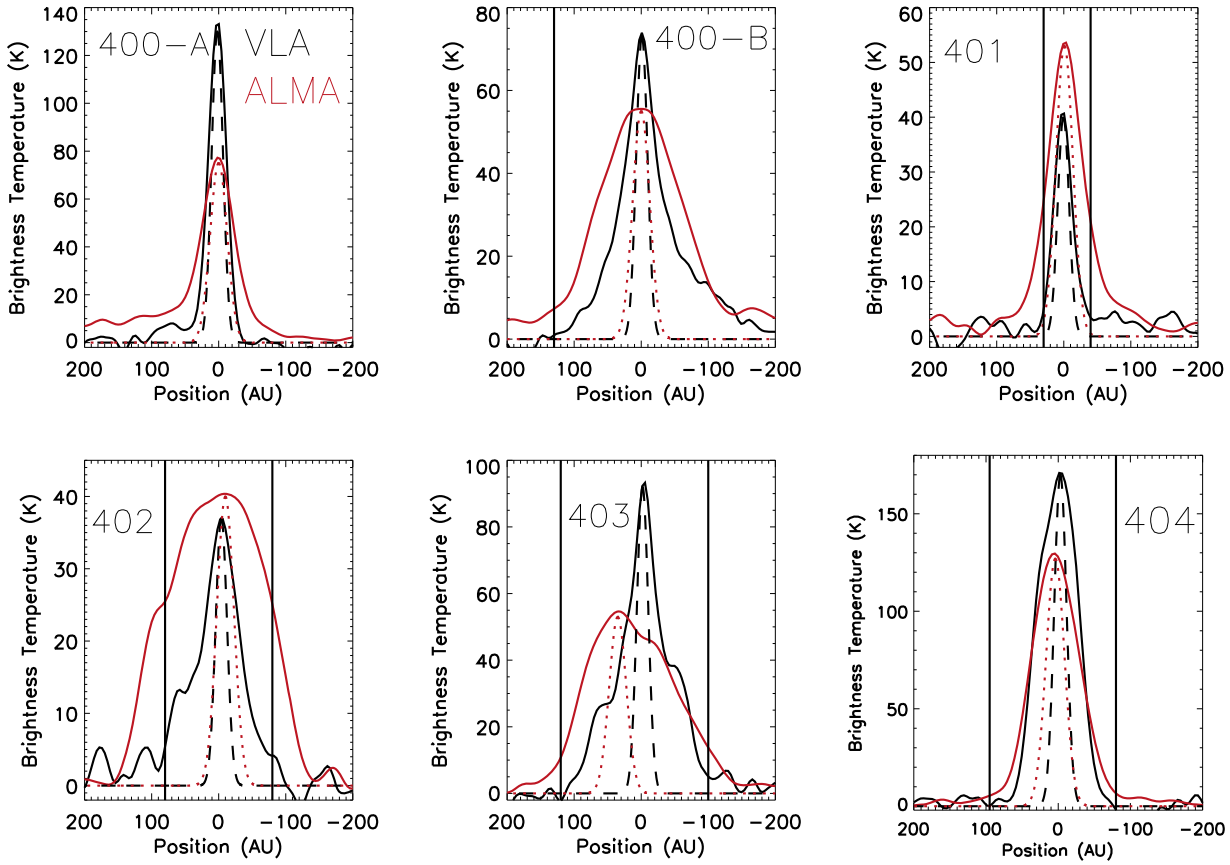

Figure 3. Brightness temperature profiles of the ALMA continuum images (red, 0.87 mm) and of the VLA continuum images (black, 8 mm) for HOPS 400-404. The cuts are made across the image in R.A. at the peak of the 8 mm emission with positive R.A. position corresponding to increasing R.A. (east on right to west on left). The red (dotted) and black (dashed) lines are the normalized beam sizes for ALMA and VLA, respectively. The solid vertical lines indicate where the 0.87 mm emission becomes optically thick ($\tau > 1$) assuming $\beta = 1$. Note that for HOPS 400-B the optically thick 0.87 mm emission occurs at −220 au and therefore is not visible in the plot.

optically thick for $\beta = 1$. Because the ratio of the 8–0.87 mm brightness temperature exceeds 0.16 over much of the detected emission, we conclude that the 0.87 mm emission is mostly optically thick toward all four of the irregular PBRs. The exact limits of the optically thick region depend on the adopted dust law.

The high optical depth at 0.87 mm is also apparent in the shapes of the cuts, which exhibit more small-scale structure at 8 mm than at 0.87 mm. Peak brightness temperatures of the 8 mm emission exceed those of the 0.87 mm emission for three of the four irregular PBRs, with HOPS 402 as the exception. Toward the peak, there is a combination of resolved and unresolved emission. The unresolved emission likely contains even higher peak brightness temperatures than the maximum values found in the maps. The high brightness temperatures at 8 mm are clear evidence of temperature gradients in HOPS 400-B, HOPS 403, and HOPS 404. A similar temperature gradient may be present in HOPS 402, but the 8 mm temperature never exceeds the 0.87 mm temperature. The presence of temperature gradients (temperature decreasing with radius) demonstrates that there is internal heating.

3.3. Temperatures, Radii, and Masses

To characterize the protostars, we estimate their average dust temperatures (T_d) at the 0.87 mm photosphere, their radii, and masses. Given the irregular shapes, we determine a half-maximum radius using $r_{\rm hm} = \sqrt{A/\pi}$, where A is the area within the half-maximum contour. To account for beam convolution, we subtract the beam radius at 400 pc in quadrature to calculate the deconvolved radius ($r_{\rm decon}$). The deconvolved radii range from 29 to 84 au (Table 2).

To estimate the dust temperature, we use the average 0.87 mm brightness temperature for pixels within the half maximum of the 0.87 mm emission and assume the 0.87 mm emission is optically thick everywhere within this contour. The resulting dust temperatures, given in Table 2, range from 33 to 95 K. These are higher than the bolometric temperatures estimated from the spectral energy distributions (SEDs) (24–44 K, Stutz et al. 2013; Furlan et al. 2016) and are higher than the typical dust temperature found in the dense gas of the Orion B cloud (16 K; Schneider et al. 2013). This is additional evidence that these sources are internally heated. If there was no internal heating, we expect dust temperatures that would be comparable to the typical dust temperature found in Schneider et al. (2013). Additionally, the SED-derived temperatures in Stutz et al. (2013) and Furlan et al. (2016) are modified blackbody model fits to single-dish data with 7″–19″ angular resolution; these contain contributions from the colder, extended envelopes surrounding the structures detected by ALMA/VLA.

We calculate the dust mass for the irregular PBRs by assuming that the 8 mm emission is optically thin. An additional assumption is that the 8 mm emission traces the dust, with a negligible free–free contribution. We adopt the average dust temperature within $r_{\rm decon}$ of the 0.87 mm emission as the overall dust temperature. The dust temperature is

Table 2
Physical Properties of Sources

HOPS ID	T_d (K)	M[a,b] ($M_\odot$)	$r_{\rm decon}$ (au)	$L_{\rm bol}$[c] ($L_\odot$)	$L_{\rm tot}$[c] ($L_\odot$)	$L_{\rm op}$ ($L_\odot$)	$T_{\rm bol}$[c] (K)	$\log(\rho)$ (g cm^{-3})	$\log(n_{\rm H_2})$ (cm^{-3})	T/U[a,b,d]
400-B	48	0.70	54.9	2.94	5.2	0.65	35	−12.22	11.11	0.018
401	39	0.11	28.7	0.61	0.75	0.08	26	−12.18	10.68	0.047
402	33	0.83	82.9	0.55	0.6	0.33	24	−12.68	10.65	0.015
403	41	1.20	84.1	4.1	5.3	0.82	44	−12.54	11.79	0.013
404	95	0.45	32.9	0.95	1.5	3.6	26	−11.75	11.59	0.032

Notes.
[a] Adopting $\kappa = 0.144$ cm^2 g^{-1} (see Section 3.3).
[b] Value scales with opacity through equation $M = (0.144\ {\rm cm^2\ g^{-1}}/\kappa_{8\ {\rm mm}}) \times M$(tabulated) (see Sections 3.3 and 4.2).
[c] Furlan et al. (2016).
[d] Scales as $T/U = \kappa_{8\ {\rm mm}}/0.144\ {\rm cm^2\ g^{-1}} \times T/U$(tabulated) (see Section 4.2).

Table 3
8 mm Dust Opacity Values from the Literature

Reference	Composition[a]	Density (cm^{-3})	Timescale (yr)	$\kappa_{8\ {\rm mm}}$ (cm^2 g^{-1})
Ossenkopf & Henning (1994)[b]	MRN no ice	10^6	10^5	0.2
Ossenkopf & Henning (1994)[b]	MRN no ice	10^8	10^5	0.76
Ossenkopf & Henning (1994)[b]	MRN with thin ice mantles	10^6	10^5	0.05
Ossenkopf & Henning (1994)[b]	MRN with thin ice mantles	10^8	10^5	0.06
Tobin et al. (2020)[c]	MRN with thin ice mantles	10^6	10^5	0.144
Woitke et al. (2016)	see reference for details	10^4–10^{14}	10^5–10^6	0.2

Notes.
[a] MRN: Mathis et al. (1977).
[b] Extrapolated to 8 mm using 1 mm and 1.3 mm points in Table 1 of Ossenkopf & Henning (1994).
[c] Extrapolated to 8 mm using the 1.3 mm opacity of 0.899 cm^2 g^{-1} with $\beta = 1$ (see Segura-Cox et al. 2016; Tychoniec et al. 2018, Tobin et al. 2020).

combined with the integrated flux density at 8 mm to calculate

$$M_{\rm dust} = \frac{F_\nu d^2}{\kappa_\nu B_\nu(T_d)}. \quad (2)$$

$B_\nu(T_d)$ is the blackbody intensity at the average dust temperature T_d from the 0.87 mm data.

As a fiducial dust opacity, we adopt $\kappa_{8.1} = 0.144$ cm^2 g^{-1}, used by Segura-Cox et al. (2016), Tychoniec et al. (2018), and Tobin et al. (2020). This value comes from the 1.3 mm opacity of 0.899 cm^2 g^{-1} (Ossenkopf & Henning 1994) extrapolated to 8.1 mm using a $\beta = 1$ as the dust opacity spectral index. The dust masses are multiplied by 100 to estimate the total gas mass presented in Table 2. The masses derived here do not include the mass in a central HSC, if present, which will be much smaller than the beam and optically thick at 8 mm. The masses may be affected by optical depth at 8 mm, which will result in an underestimate of the mass, and by higher temperatures in the opaque regions, which will result in an overestimate.

The largest uncertainty in the masses comes from the range of possible dust opacities. We give a plausible range of κ values in Table 3 using different dust laws in the literature. Our fiducial dust law falls above the Ossenkopf & Henning (1994) dust law with an initial Mathis et al. (1977, hereafter MRN) size distribution, thin ice mantles, and a gas density of 10^6 cm^{-3}, this law gives a kappa value of 0.05 cm^2 g^{-1} when extrapolated to 8 mm and increases the resulting masses of the optically thick regions by a factor of ∼3. On the opposite end, extrapolating the Ossenkopf & Henning (1994) law for an initial MRN distribution, no ice, and a gas density of 10^8 cm^{-3} yields $\kappa = 0.76$ cm^2 g^{-1}, which lowers the resulting mass by a factor of ∼5.

Clearly, the adopted opacity law will change the resulting mass and influence the interpretation of the irregular PBRs. We conclude that the uncertainty in mass from the dust law is over one order of magnitude. Further uncertainties in the mass may come from variations in the gas-to-dust ratio—we adopt 100:1—and adopted dust temperature (e.g., Bate & Lorén-Aguilar 2017). The footnotes of Table 2 describe how the calculated values vary with the adopted opacity, and we discuss the implication of this range in the next section. We note that the masses calculated with the optically thick 0.87 mm data tabulated in Tobin et al. (2020) underestimate the more accurate masses calculated with the 8 mm using the same dust law ($\kappa = 0.144$ cm^2 g^{-1}).

3.4. Luminosities and Timescales

The $L_{\rm bol}$- (integrated SED including both internal and external heating) and $L_{\rm tot}$- (luminosity from model fits including corrections for foreground extinction and beaming by outflow cavities) derived luminosities for the protostars given by Furlan et al. (2016) range from 0.6 to 2.9 $L_\odot$ and from 0.6 to 5.3 $L_\odot$, respectively (Table 2). Note that $L_{\rm tot}$ makes assumptions about the structure of the protostellar envelope as well as the lack of external heating, which may not be appropriate for the four irregular PBRs. Additionally, we estimate the luminosities emitted by the optically thick regions from their measured dust temperatures and sizes, assuming a spherical geometry with a constant radius at all wavelengths.

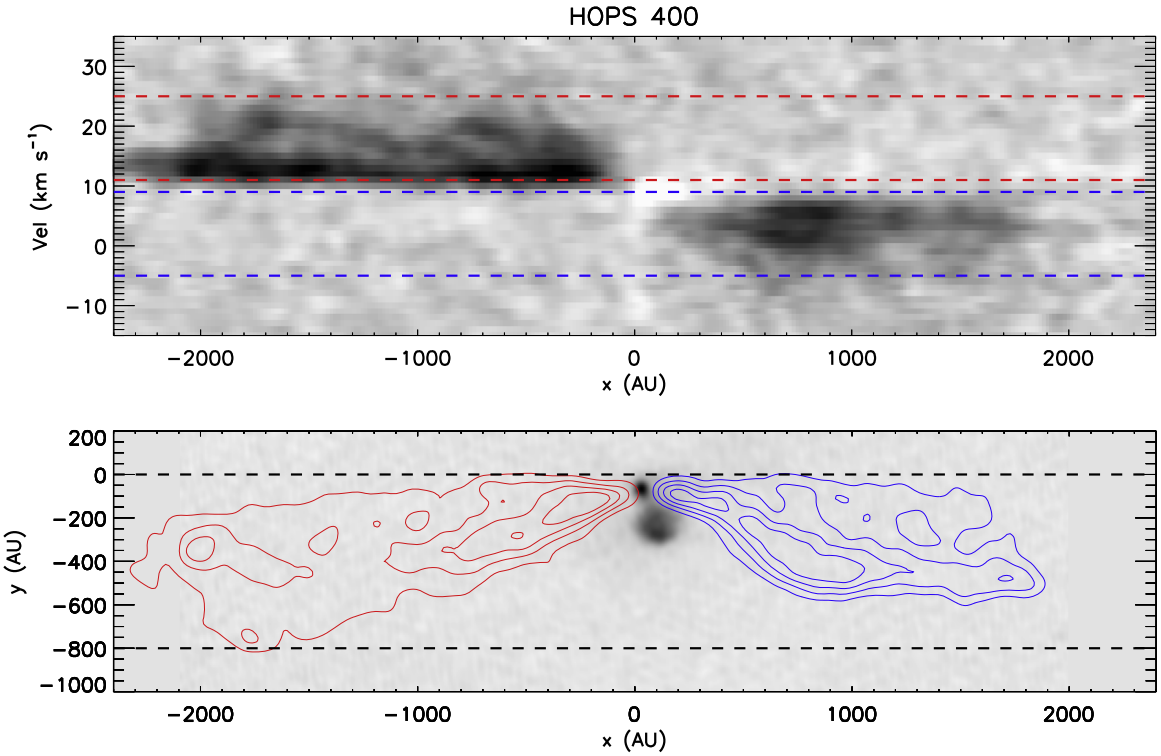

Figure 4. HOPS 400: ALMA ^{12}CO ($J = 3$–2) position–velocity diagram (top) and 0.87 mm continuum image (grayscale) with red- and blueshifted integrated intensity contours at [20, 40, 60, 80] mJy beam^{-1} km s^{-1} (bottom). The compact outflow is centered on the continuum of 400-A and is confined to regions near the protostar. The contours are the integrated emission in the velocity ranges −5 to 9 km s^{-1} for the blue lobe and 11–25 km s^{-1} for the red lobe. The red and blue dashed lines in the *PV* diagram (top) show the velocity integration range on the *y*-axis. The black dashed lines in the outflow contour plot (bottom) show the *y*-axis spatial range integrated over the *PV* diagram. A rotation angle of −27° was implemented with respect to the PA rotation of the *y*-axis.

This luminosity is given by

$$L_{\rm op} = 4\pi\sigma r_{\rm decon}^2 T_d^4, \quad (3)$$

where $r_{\rm decon}$ is the deconvolved radius and T_d is the adopted dust temperature. The resulting luminosities range from 0.08 to 3.61 $L_\odot$ (Table 2). HOPS 404 has the largest $L_{\rm op}$ due to the highest dust temperature where $L_{\rm op}$ exceeds the values of $L_{\rm bol}$ and $L_{\rm tot}$. This may result from an underestimate in the amount of foreground extinction and the degree of beaming of the luminosity by the outflow cavity in the determination of $L_{\rm tot}$. Alternatively, the simple spherical, constant temperature geometry assumed by $L_{\rm op}$ may overestimate the flux. We note that in the case of HOPS 400, the SED and model fit luminosities are for the combined system, while $L_{\rm op}$ is for HOPS 400-B alone.

We also calculate two timescales in Table 4. The first is the freefall timescale, $t_{\rm ff} = (3\pi/32{\rm G}\rho)^{0.5}$, which is determined assuming $\rho = 3{\rm M}/4\pi r_{\rm decon}^3$ with the values in Table 2. The resulting high densities, i.e., $>10^{-13}$ g cm^{-3}, put these sources at the critical point where the emission should be optically thick to their own radiation (Masunaga et al. 1998). The resulting freefall timescales are all less than 150 yr (Table 4).

A second timescale is a cooling time and gives the rate of contraction for a given mass and radius assuming that all the heating due to contraction is radiated away. This is given by the Kelvin–Helmholtz time for luminosity, L,

$$t_{\rm KH} = \alpha\frac{GM^2}{LR}, \quad (4)$$

Table 4
Timescales of Collapse, Contraction, and Lifetime

HOPS ID	$t_{\rm ff}$[a,b] (yr)	$t_{\rm KH}$[a,c] ($L_{\rm bol}$) (yr)	$t_{\rm KH}$[a,c] ($L_{\rm tot}$) (yr)	$t_{\rm KH}$[a,c] ($L_{\rm op}$) (yr)	$t_{\rm stat}$ (yr)
400-B	86	440	250	2000	6000
401	82	100	80	480	⋯
402	146	2200	2000	3600	6000
403	125	600	465	3000	6000
404	50	930	590	250	6000

Notes.
[a] Adopting $\kappa = 0.144$ cm^2 g^{-1} (see Section 3.3).
[b] Value scales with opacity by equation $t_{\rm ff} = (\kappa_{8\ {\rm mm}}/0.144\ {\rm cm^2\ g^{-1}})^{1/2} \times t_{\rm ff}$(tabulated) (see Section 3.4).
[c] Value scales with opacity by equation $t_{\rm KH} = (0.144\ {\rm cm^2\ g^{-1}}/\kappa_{8\ {\rm mm}})^2 \times t_{\rm KH}$(tabulated) (see Section 3.4).

where we assume $\alpha = 3/5$ for a constant density sphere. Adopting $L_{\rm op}$ results in times ranging from 250 to 3600 yr. Adopting $L_{\rm bol}$ from Furlan et al. (2016), the $t_{\rm KH}$ range from 440 to 2200 yr, and adopting $L_{\rm tot}$ yields 250–2000 yr (Table 4). For all the irregular PBRs, except HOPS 404, the $t_{\rm KH}$ are consistently longer than the freefall times. These values, however, depend the mass, which in turn depend strongly on the adopted opacity law (Table 3). We discuss the ranges of plausible values and their implications in Section 4.

3.5. Outflow Properties

Here we highlight the outflow properties of each source that has a detection in the ^{12}CO ($J = 3$–2) ALMA channel maps:

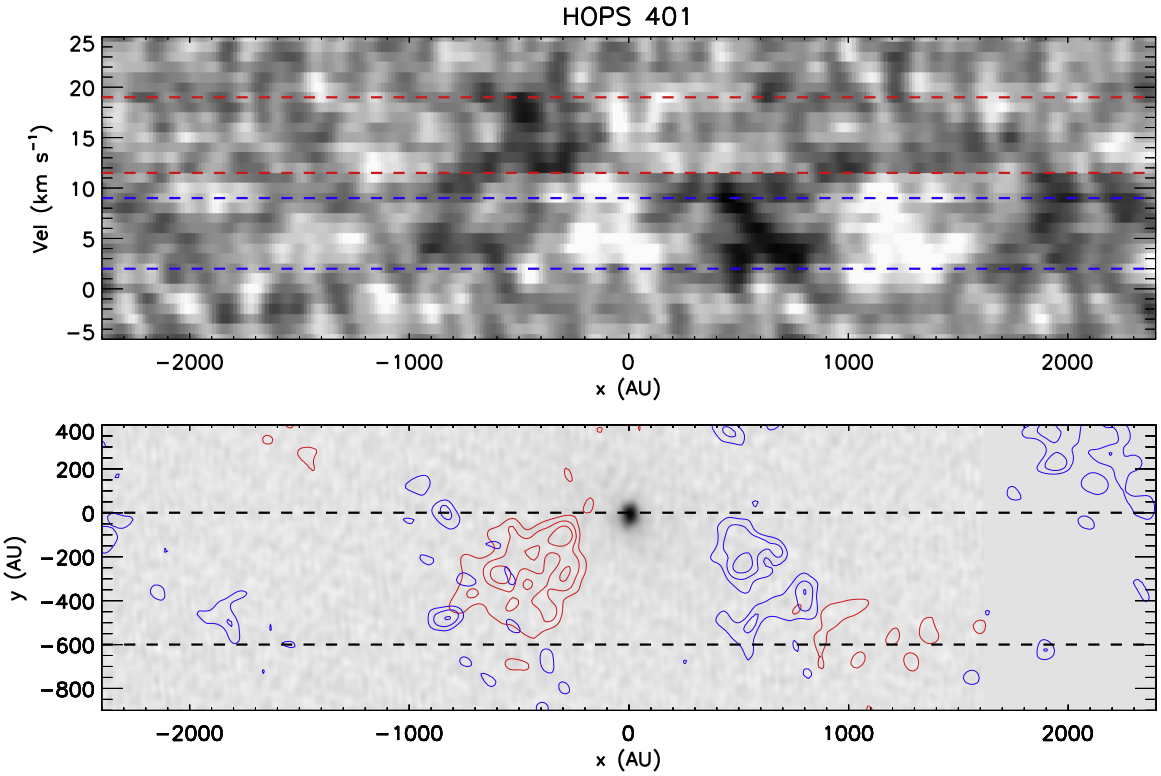

Figure 5. HOPS 401: ALMA ^{12}CO ($J = 3$–2) position–velocity diagram (top) and 0.87 mm continuum image (grayscale) with red- and blueshifted integrated intensity contours at [40, 60, 80] mJy beam^{-1} km s^{-1} (bottom). The contours are the integrated emission in the velocity ranges 2–9 km s^{-1} for the blue lobe and 11–19 km s^{-1} for the red lobe. The red and blue dashed lines in the *PV* diagram (top) show the velocity integration range on the *y*-axis. The black dashed lines in the outflow contour plot (bottom) show the *y*-axis spatial range integrated over the *PV* diagram. A rotation angle of 315° was implemented with respect to the PA rotation of the *y*-axis.

HOPS 400-A, HOPS 401, HOPS 403, and HOPS 404 (Figures 4–7). This is the first detection of an outflow from HOPS 404 and potentially HOPS 401. HOPS 400-A and HOPS 403 were previously found by CARMA observations by Tobin et al. (2015, 2016), with HOPS 401 and HOPS 404 being nondetections at their sensitivities.

The outflow masses are calculated using the LTE approximation following the method in Yıldız et al. (2015) and assume a gas temperature of 70 K. We calculate the outflow force F_{CO} using the method in van der Marel et al. (2013) assuming an inclination of 50°. The systemic velocities of the PBRs are ∼10 km s^{-1}, and we use the highest velocity emission channels of each lobe in the force equation. The calculated properties of the outflows are listed in Table 5. We do not have inclinations for each individual outflow. Therefore, we report the projected lengths (a lower limit to the actual length) and the radial velocities (also a lower limit). The resulting dynamical times assume a 50° inclination, with the times being lower with higher inclinations and higher with lower inclinations.

The HOPS 400-A and HOPS 403 outflows have the longest lengths and the largest masses and forces in each lobe. The highest velocity emission is also in HOPS 400-A and HOPS 403. In the case of HOPS 403, the continuum is opaque (Figure 6), and we cannot trace the outflow to its driving source. The bright, point-like source in HOPS 403 at 8 mm is the likely source of the outflow. Because HOPS 403 is optically thick, we cannot tell whether this point source is inside the opaque, irregular region or a companion located behind it. The presence of a companion behind HOPS 403 would explain why L_{tot} and L_{bol} of HOPS 403 are more than six times higher than the luminosity for the opaque region (Table 2).

The masses of the outflow lobes in HOPS 400-A and 403 are within an order of magnitude of Tobin et al. (2016). In contrast, Tobin et al. (2016) found lengths of the outflow lobes and dynamical times three times larger for HOPS 403 and 400-A; the ALMA data are unable to recover the large-scale outflow emission that CARMA did. The resulting values for the times are consistent with young outflows from either FHSCs or Class 0 protostars. We note that other outflow tracers (e.g., H_2CO) may pick up additional material that is not detected by the observations presented here and shed more light on the outflows.

In HOPS 404 (Figure 7), the masses of each lobe are the smallest, the lengths the shortest, the forces the lowest, and the maximum velocities are only 2 km s^{-1}. We discuss the implications for this in Section 4. A more detailed description of all of the outflows is given in the Appendix.

4. Discussion

We have resolved four irregular protostars that are optically thick at 0.87 mm over ∼100 au diameter regions, each showing peaks that may be optically thick at 8 mm within ∼50 au diameter regions. We interpret these as the centers of collapsing molecular fragments that are optically thick at their peak wavelength of ∼30 μm, which corresponds to a temperature of ∼100 K. Models of collapsing fragments show that due to the very high densities of gas in these opaque regions, ∼10^{-13} gm cm^{-3}, the heating generated by compression exceeds the

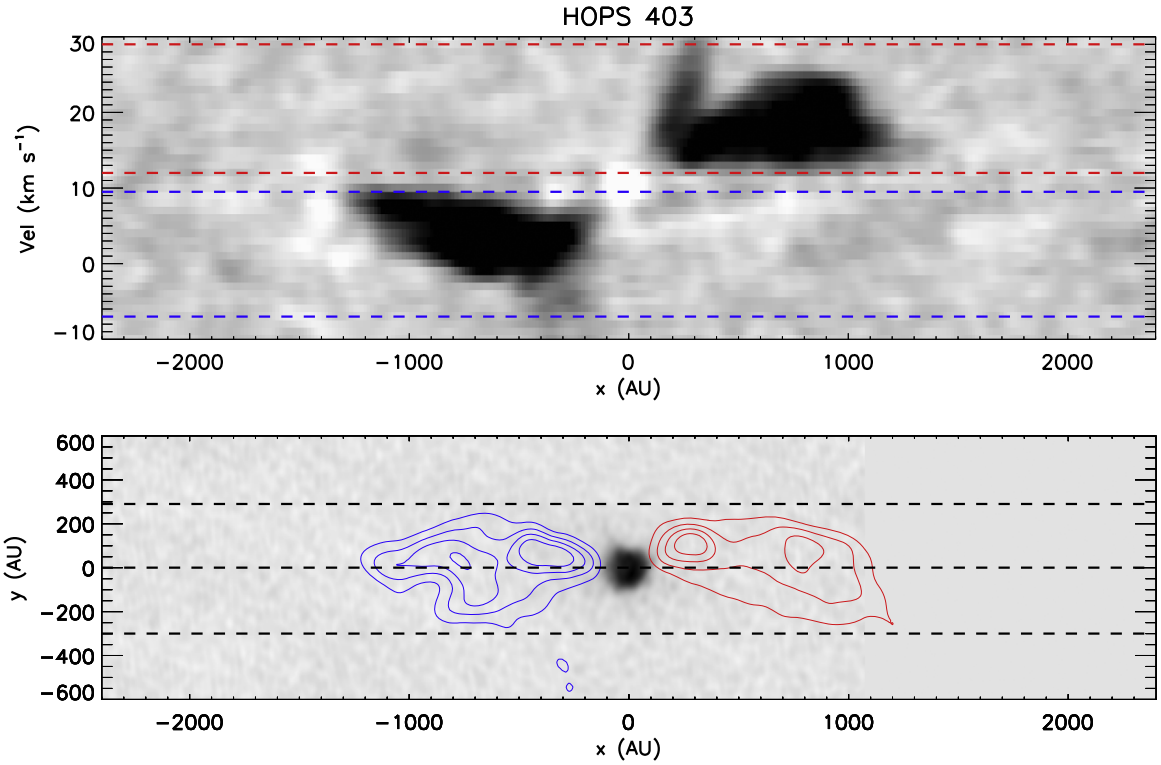

Figure 6. HOPS 403: ALMA ^{12}CO ($J = 3$–2) position–velocity diagram (top) and 0.87 mm continuum image (grayscale) with red- and blueshifted integrated intensity contours at [20, 40, 60, 80] mJy beam^{-1} km s^{-1} (bottom). The compact outflow is centered on the continuum of HOPS 403 and is confined to regions near the protostar, but it is not detected within the continuum due to the high optical depth at 0.87 mm. The contours in the integrated intensity plot are −7 to 9.5 km s^{-1} for the blue and 12–29 km s^{-1} for the red. The red and blue dashed lines in the *PV* diagram (top) show the velocity integration range on the *y*-axis. The upper and lower black dashed lines in the outflow contour plot (bottom) show the *y*-axis spatial range integrated over the *PV* diagram. The middle dashed line is the *y*-axis center of the continuum image. A rotation angle of −27° was implemented with respect to the PA rotation of the *y*-axis.

rate of cooling by radiation (Masunaga et al. 1998). Within this thermal opacity horizon, the collapsing gas is no longer isothermal, and the ensuing increase in temperature and pressure will slow and eventually halt collapse. The high optical depth, and the resulting adiabatic equation of state, should also resist fragmentation despite the presence of multiple Jeans masses within each region (Low & Lynden-Bell 1976; Rees 1976; Silk 1977). In this way, the formation of an optically thick zone is the prelude to the formation of an HSC, and these objects may trace the earliest observable state of protostar formation. While the ALMA 0.87 mm data measure the sizes and temperatures of the opaque horizons, the VLA data, due to the lower optical depth at 8 mm, resolve the structures that are opaque at shorter wavelengths. These data show irregular, noncircularly symmetric structures with bright, compact peaks. Although we refer to these objects as protostars, we do not know if they all contain HSCs; the presence of such a central core is often implied in the standard usage of the term protostar.

Analogous sources have been identified in other nearby star-forming regions. Hernández-Gómez et al. (2019) find that source B in the binary Class 0 protostar IRAS 16293–2422 has a power-law spectrum ($S_\nu \propto \nu^{2.28}$) from 0.5 mm to 10 cm. They argue that the observations are tracing dust emission out to 10 cm and that the dust becomes optically thick at the shorter wavelengths. In the Perseus molecular cloud, Cox et al. (2015) find that source A1 of the NGC 1333 IRAS 4A system has an optically thick inner core, and Sahu et al. (2019) detect complex organic molecules in absorption against the continuum. The sample presented in this paper is the result of the first systematic search for such extended, irregular optically thick regions utilizing the large population found in Orion, the well-characterized SEDs of the HOPS program, and the high-resolution ALMA and VLA maps from the VANDAM Orion survey.

Simulations of fragment collapse predict the formation of optically thick regions that are (i) several astronomical units in size, (ii) thermally supported, (iii) and with masses $<0.1\ M_\odot$ (e.g., Bhandare et al. 2018). These objects are the FHSCs first described by Larson (1969). Only simulations invoking large amounts of rotational energy, resulting in the formation of highly flattened prestellar disks instead of spherical HSCs, predict masses and radii comparable to those of the envelopes (Bate 2011; Commerçon et al. 2012). As we will discuss in the remainder in this section, there are several areas of tension between the observed results and existing models.

4.1. The Statistical Lifetime

The detection of only four irregular, optically thick protostars out of a sample of 328 protostars places constraints on the lifetime of such objects, i.e., $t_{\rm stat}$. If we assume (i) that the formation of extended, opaque zones is an early stage all protostars go through and (ii) that the star formation rate is constant over a protostellar lifetime, the duration of this stage can be estimated from the ratio of the number of extended sources over the total number of protostars. For a protostellar lifetime of 0.5 Myr (Dunham et al. 2014), the duration is $t_{\rm stat} = 4/328 \times 0.5\,{\rm Myr} \approx 6000\,{\rm yr}$. It is possible that the assumptions in $t_{\rm stat}$ are incorrect, e.g., Kristensen & Dunham (2018). Using the binomial theorem, we determine the

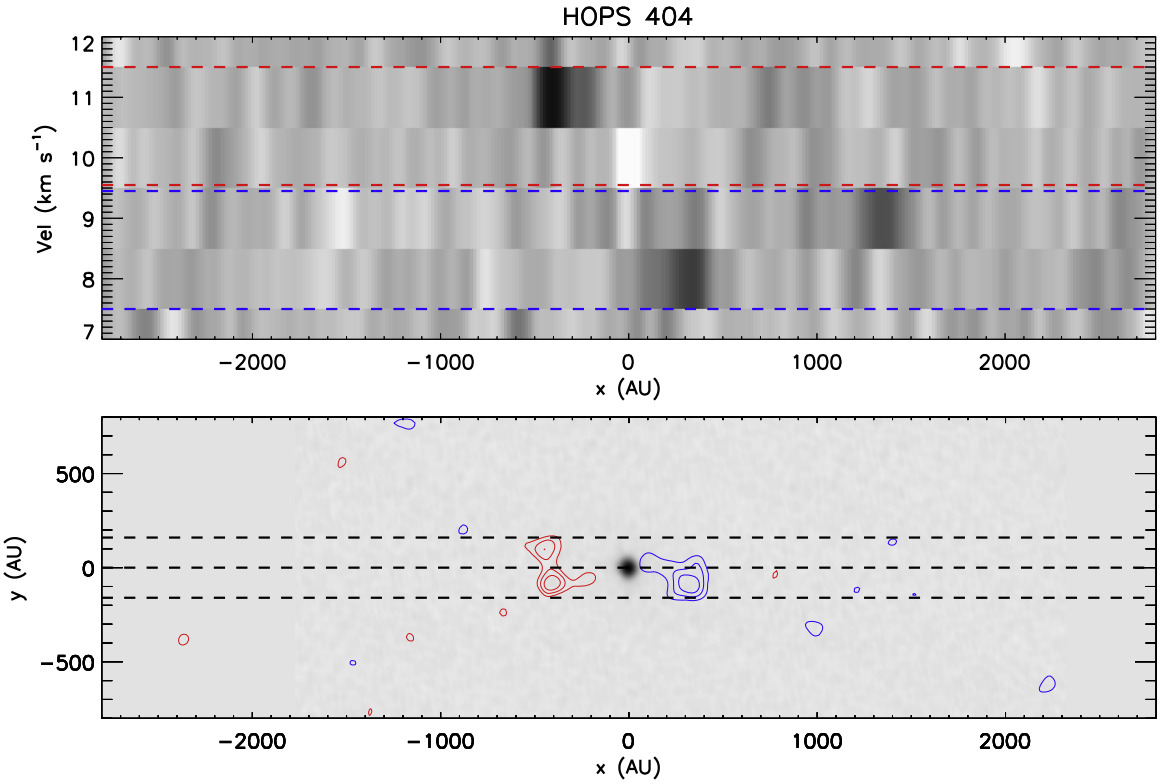

Figure 7. HOPS 404: ALMA ^{12}CO ($J = 3$–2) position–velocity diagram (top) and 0.87 mm continuum image (grayscale) with red- and blueshifted integrated intensity contours at [40, 60, 80] mJy beam^{-1} km s^{-1} (bottom). The compact outflow is centered on the continuum of HOPS 404 and is confined to regions near the protostar. The contours are the integrated emission in the velocity ranges 7.5–9.5 km s^{-1} for the blue lobe and 9.5–11.5 km s^{-1} for the red lobe. The red and blue dashed lines in the *PV* diagram (top) show the velocity integration range on the *y*-axis. The upper and lower black dashed lines in the outflow contour plot (bottom) show the *y*-axis spatial range integrated over the *PV* diagram. The middle dashed line is the *y*-axis center of the continuum image. A rotation angle of 35° was implemented with respect to the PA rotation of the *y*-axis.

Table 5
Outflow Properties of Sources

HOPS ID	M_{red}/M_{blue} (10^{-3} $M_\odot$)	$t_{dyn,red}/t_{dyn,blue}$[a] (yr)	F_{red}/F_{blue} ($M_\odot$km s^{-1} yr^{-1})	R_{red}/R_{blue} (au)	V_{red}/V_{blue} (km s^{-1})
400-A	3.2/3.0	825/525	$1.95 \times 10^{-4}/2.38 \times 10^{-4}$	2454/2018	+24/-8
401	1.6/0.26	360/310	$6.44 \times 10^{-5}/1.02 \times 10^{-5}$	680/720	+19/+1
403	4.1/3.9	316/316	$4.40 \times 10^{-4}/4.46 \times 10^{-4}$	1200/1200	+29/−7
404	0.02/0.03	1710/1105	$1.35 \times 10^{-7}/2.48 \times 10^{-7}$	680/483	+12/+8

Note.
[a] $t_{dyn,red} = R_{red}/(V_{red,max}-V_{LSR})$, $t_{dyn,blue} = R_{blue}/(V_{blue,max}-V_{LSR})$, where R_{red} and R_{blue} are the maximum detected extent from the central source.

cumulative probability distribution for finding four optically thick sources as a function of the lifetime of the optically thick stage (Figure 8). This figure shows the distribution of probabilities as a function of lifetime and demonstrates that lifetimes under 1000 yr have very low chances (<1%) of producing four distinct objects within the Orion sample. The length of the optically thick stage of 6000 yr is comparable to the t_{KH} lifetime, particularly when adopting the luminosities of the optically thick region (L_{op}) in Section 3.4.

4.2. Inside the Opacity Horizon

If these objects are tracing the transition of a collapsing opaque region to a protostar, the structure, kinematics, and thermodynamics of the gas within the opaque zones are essential for understanding the conditions that lead to the formation of the HSCs and guide their early (<10,000 yr) evolution. Due to the high optical depths and limited sensitivity in the 0.87 mm band, we do not detect molecular lines that can be used to directly observe the motions of the gas. Instead, we must infer the possible state of the gas from the masses, radii, and luminosities.

To do this, we compare t_{ff}, t_{KH}, and t_{stat}. Both t_{ff} and t_{KH} are a function of the mass and radius, while t_{KH} is also dependent on the luminosity (see footnotes of Table 4). The value of t_{stat} is independent of the derived physical parameters. We show the dependence of the three timescales on mass, which varies with the adopted dust opacity, in Figure 9. Here we find that there are no masses where all three timescales are equal. Low masses are needed for $t_{ff} \approx t_{KH}$, while high masses are needed for $t_{KH} \approx t_{stat}$.

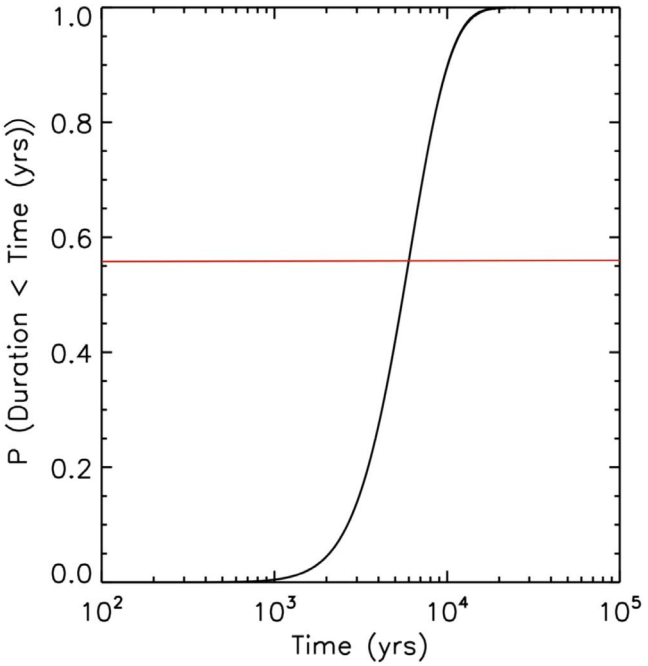

Figure 8. The probability of detecting four optically thick protostars vs. the lifetime of the optically thick phase. Each value of the probability corresponds to a different lifetime. The lifetime of the optically thick phase is the number of optically thick sources observed divided by the total number of protostars and multiplied by the total protostellar lifetime of 0.5 Myr (Dunham et al. 2014). The red horizontal line indicates the probability of the protostars having a mean lifetime of 6000 yr or less.

There are no plausible masses where $t_{\rm ff} \approx t_{\rm stat}$. This suggests that the collapse is not on a freefall timescale. Indeed, for higher masses, we find that $t_{\rm KH} \approx t_{\rm stat}$, while both are an order of magnitude higher than $t_{\rm ff}$. This would suggest that the opaque zones may not be in freefall but are slowly contracting as they radiate away their thermal energy. The difficulty with this interpretation is that the thermal pressure is insufficient to support the opaque zones against collapse. This is demonstrated in Figure 10 and the last column of Table 2, where we compare the gravitational potential energy, U, to the kinetic energy, T, as a function of the adopted mass. Here we assume that the opaque zones can be approximated as constant density spheres with the radii given in Table 2 and no external pressure. We calculate the thermal energy using the temperatures in Table 2. The zones are in virial equilibrium when $2T = U$. We also plot curves equal to $4T$ and $6T$; these would represent cases where there is equipartition between the thermal and turbulent energies or equipartition among the thermal, turbulent, and magnetic energies, respectively. In none of the three cases do we find a mass where the opaque regions can be in virial equilibrium and $t_{\rm stat}$ can be satisfied. Given the lack of a consistent model, we consider four different scenarios below.

4.2.1. The Gas is in Freefall

The simplest scenario is that the opaque regions are in freefall with lifetimes of only a few hundred years. In the case where the masses are at the low end of the plausible mass range, $t_{\rm ff}$ and $t_{\rm KH}$ can be similar. These smaller masses require either large grains to increase the dust opacity or temperatures that exceed the measured values by a factor of a few. If the former is correct, the dust opacity must be larger than the values of $0.144\,{\rm cm^2\,g^{-1}}$ and $\beta = 1$ adopted for the fiducial masses given in Table 2. This opacity already attempts to account for a significant degree of grain growth over a $\beta = 1.8$ model. Thus, substantial additional grain growth would need to happen in the starless fragment stage prior to the onset of HSC formation. In order for grains to grow to millimeter size, very high densities over 100,000 yr timescales need to be maintained (Table 3; Ossenkopf & Henning 1994; Ormel et al. 2011), and it is not clear that the presence of such large grains is realistic. The presence of such large grains would also imply that the regions where the 0.87 mm emission is optically thick are smaller than shown in Figures 2 and 3, which may have detectable consequences, particularly for future molecular-line observations. Future extensions of the continuum measurements to longer wavelengths will also put additional constraints on grain size distribution in these sources.

Alternatively, the gas may be in freefall but $t_{\rm KH} > t_{\rm ff}$; in this case, the opaque zones will rapidly heat up as they are compressed until the increasing central pressure is able to halt or slow collapse. In either case, the implied lifetimes are not consistent with $t_{\rm stat}$, and either this is a very unlikely coincidence, the statistical probability of observing four such regions in freefall is <1%, or $t_{\rm stat}$ is not representative of the lifetimes of these sources.

4.2.2. Turbulence Resists Collapse

If the statistical lifetime is correct, then these opaque regions cannot be in a state of freefall. In this case, the contraction times implied by the measured luminosities require masses toward the higher end of the mass range. Furthermore, additional support is required to keep the large masses within the opacity horizon from collapsing or to slow down the rate of collapse.

We first consider whether turbulence can supply that support. This can be quantified by considering the virial theorem for the central opaque zones (McKee 1999; Hartmann 2009):

$$3\frac{MkT}{\mu m_{\rm H}} + 3M\sigma_{\rm turb}^2 + W = \frac{3}{5}\frac{GM^2}{R} + \int_S P\,\boldsymbol{r}\cdot\boldsymbol{dS}, \qquad (5)$$

where $\sigma_{\rm turb}$ is the turbulent line width, R is the radius of the opaque zone, M is the enclosed mass, P is the surface pressure at the opacity horizon, and W is the magnetic term that we will discuss in the following scenario. Ignoring the surface pressure and magnetic terms, we estimate that turbulent velocities of $\sim 1.3\,{\rm km\,s^{-1}}$ are required, assuming virial equilibrium and adopting the radius and mass in Table 2 for HOPS 402. Compared to the sound speed of $0.34\,{\rm km\,s^{-1}}$, the velocities are supersonic. These motions would dissipate on a crossing time (Mac Low et al. 1998), $t_{\rm cross} = R/\sigma_{\rm turb}$, where $t_{\rm cross} = 300\,{\rm yr}$ for HOPS 402, and the turbulent support would dampen in a few hundred years.

One possible way of sustaining turbulence may be the input of energy by infall from the surrounding envelope of gas. Klessen & Hennebelle (2010) propose that accretion may be a universal mechanism for driving turbulence. The line width that can be sustained is given by

$$\sigma_{\rm turb} = \left(2\epsilon R v_{\rm infall}^2 \frac{\dot{M}}{M}\right)^{1/3}, \qquad (6)$$

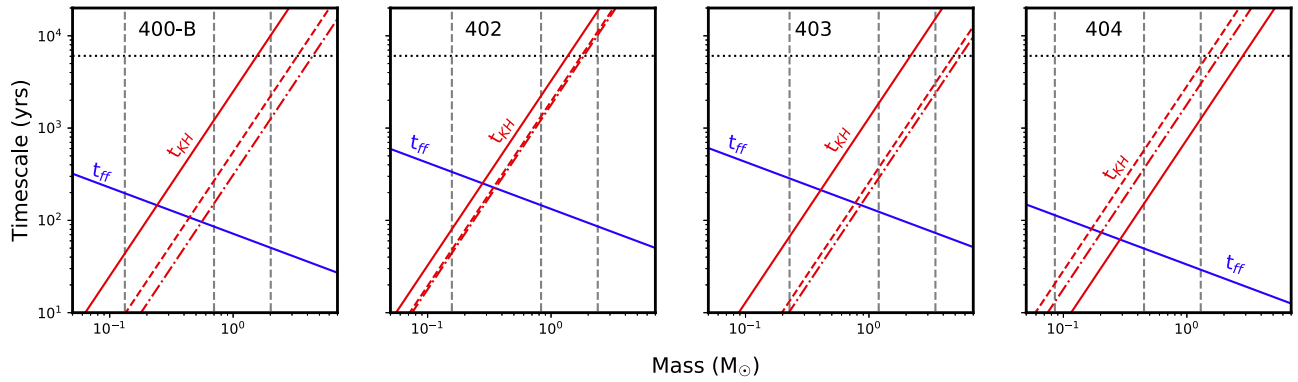

Figure 9. The timescale for collapse vs. mass for HOPS 400-B, HOPS 402, HOPS 403, and HOPS 404. The blue line is the $t_{\rm ff}$ while the red lines are $t_{\rm KH}$ for the $L_{\rm op}$ (solid), $L_{\rm bol}$ (dashed), and $L_{\rm tot}$ (dotted–dashed). The horizontal dotted line is $t_{\rm stat} = 6000$ yr, while the vertical lines give the minimum, fiducial, and maximum masses based on the opacity laws in Table 3.

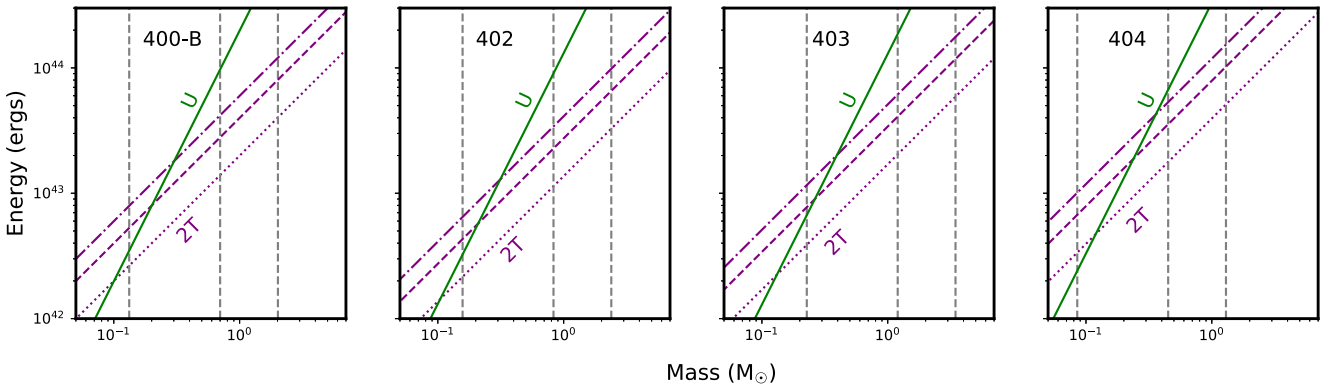

Figure 10. The energy vs. mass for HOPS 400-B, HOPS 402, HOPS 403, and HOPS 404. The green line is the potential energy U while the purple lines are multiples of the kinetic energy T, specifically $2T$ (dotted), $4T$ (dashed), and $6T$ (dotted–dashed). These represent twice the thermal energy alone, twice the thermal and turbulent energy in equipartition, and twice the thermal, turbulent, and magnetic energy in equipartition. In virial equilibrium, these lines would intersect the line for U. As in Figure 9, the vertical lines give the minimum, fiducial, and maximum masses for the range of dust opacities.

where $v_{\rm infall}$ is the infall rate and ϵ is an efficiency factor that we set to 0.1 (Heitsch 2013). For an infall rate of $10^{-4}\ M_\odot\ {\rm yr}^{-1}$ (Stutz et al. 2013; Furlan et al. 2016), the resulting line width is $\sigma_{\rm turb} = 0.6\ {\rm km\ s}^{-1}$. This shows that the estimated infall rate, although high for low-mass protostars, is insufficient to drive the required level of supersonic turbulence. For the protostars with outflows or companions with outflows, it is possible that the outflow is driving the turbulence (Offner & Liu 2018); however, for protostars without outflows it is unlikely that the turbulence can be sustained for more than a few hundred years.

4.2.3. Magnetic Fields Help Resist Collapse

An alternative form of support can be magnetic fields. In Equation (5), this term is given as

$$W = \int_V \frac{B^2}{8\pi} dV + \int_S \boldsymbol{r} \cdot \left(\boldsymbol{BB} - \frac{1}{2} B^2 \boldsymbol{I} \right) \cdot \boldsymbol{dS}, \qquad (7)$$

where I is the unit tensor. As discussed in Hartmann (2009), the collapse of a gas fragment requires that the magnetic term in the virial theorem be less than the potential energy term (U) as both the magnetic and potential energy terms scale approximately as $1/R$ as the fragment shrinks, assuming the magnetic field is frozen to the gas.

It has been found, though, that the magnetic energy can exceed thermal and turbulent energies. Magnetic field energies that dominate the turbulent and kinetic energies, but not the potential energy, have been found for the high-mass protostars G9.62+0.19 and G31.41+0.31 (Girart et al. 2009; Dall'Olio et al. 2019). A magnetic field that is dominated by gravity, but not turbulent motions, can produce the hourglass-shaped magnetic fields observed toward low-mass protostars and starless cores (Myers et al. 2018). Furthermore, on large scales, Stutz & Gould (2016) found that in the integral-shaped filament (ISF) in Orion A, the potential energy dominates on large scales, while magnetic energy density dominates on small scales; moreover, in subsequent work, González Lobos & Stutz (2019) show that the turbulent energy is insufficient to support the ISF.

If the magnetic field dominates over the total kinetic energy, but not the gravitational energy, the increase in temperature at high densities will boost the thermal energy and, by raising the sound speed, also elevate the sub/transonic turbulent motions. This boost in thermal and turbulent motions increases the support against collapse. In this way, it is possible that the support of the opaque zone can be primarily—but not solely—due to the magnetic field. One caveat is that strong magnetic fields often lead to flattened structures in models (e.g., Commerçon et al. 2012); this is inconsistent with the observed

morphologies of the opaque zones, unless seen face on (see next scenario).

4.2.4. Rotational Support and Disks

Rotational motion can also provide support against collapse in cases where the rotational energy is high, producing extended disks (Bate 1998; Saigo et al. 2008). Bate (2011) simulated the collapse of a 1 $M_{\odot}$, uniform density, uniformly rotating sphere with rotational to gravitational energy ratios ranging from 0 to 0.04. While the low value resulted in hydrostatically supported FSHCs a few astronomical units in diameter, the larger values led to rotationally supported prestellar disks that extend to radii of 150 au, have masses approaching 0.2 $M_{\odot}$, and lifetimes extending to 3000 yr (Figure 15 from Bate 2011). The temperatures and densities of the simulated prestellar disks are also similar to those of the irregular protostars. The irregular morphologies may arise from gravitational instabilities in the disks.

The primary difficulty with rotational support is that models invoking rotation predict highly flattened morphologies. The aspect ratios of the irregular structures are close to 1, particularly when considering the outer contours of the 0.87 mm emission. This suggests that they would need to be observed at a nearly face-on inclination if they were prestellar disks. It is possible (although quite unlikely) that all four irregular PBRs are observed at this inclination, but there are other difficulties with purely rotational support. In particular, the orientation of the outflows in HOPS 404 and 403, if not a binary, would rule out a face-on orientation if the outflows are oriented perpendicular to the disks.

Although disks remain a plausible explanation, it is very unlikely that irregular protostars are stable Keplerian disks surrounding protostars, i.e., young Class 0 protostars with massive disks. Again, the aspect ratios of ~1 for the observed disks would imply that the disks are observed at nearly face-on inclinations. At such inclinations, the SEDs would be less red than typical Class 0 protostars due to the lower extinction along the angular momentum axis (Furlan et al. 2016). In contrast, the PBRs are distinguished by their low $T_{\rm bol}$ and weak mid-IR emission compared to other Orion Class 0 protostars (Stutz et al. 2013). Furthermore, the red and blue outflow lobes of a face-on protostar would overlap, which is not the case for the observed outflows. Finally, the irregular sources do not look like the disks resolved around many protostars in the VANDAM sample (Tobin et al. 2020).

As we will discuss in the next section, it is likely that one to two of the opaque regions, HOPS 404 and potentially HOPS 403, contains HSCs. These HSCs may have formed in prestellar disks (e.g., Bate 2011) or, perhaps, formed before the disks. In both cases, the irregular structures, high masses, and off-centered peaks observed at 8 mm suggest that the disks would have masses similar to or higher than those of the HSCs. The opaque regions may also contain smaller, more stable disks; these could be responsible for the observed outflows.

4.3. Outflows as Tracers of Hydrostatic Cores

Although fragmentation of the high-opacity, adiabatic gas may be suppressed compared to that of the isothermal gas (e.g., Silk 1977), models show the formation of denser objects within the high-opacity zones. In prestellar disks, gravitational instabilities lead to the formation of multiple HSCs (Bate 2011), although this fragmentation can be suppressed by magnetic fields (Commerçon et al. 2012). Even for hydrostatically supported FHSCs, the dissociation of H_2 in the centers of the HSCs leads to the formation of second hydrostatic cores (i.e., protostars) inside the FHSCs (e.g., Larson 1969; Basu & Mouschovias 1994).

Within the observed opacity horizons, there is evidence that HSCs have formed. The VLA maps show compact peaks that are potentially optically thick at 8 mm and could contain HSCs. Furthermore, the presence of outflows from HOPS 404, and possibly from HOPS 403, suggest the presence of HSCs (i.e., young stellar objects) whose gravity is needed to generate outflows.

The outflow properties derived in Section 3.5 place constraints on the mass and radius of the objects driving the outflows. The outflows are likely driven by the coupling of magnetic fields to disk rotation, and therefore the maximum velocity of the outflow is proportional to the escape velocity from the HSC,

$$v_{\rm out} = \frac{R_a}{R_0} v_{\rm esc} \tag{8}$$

(Equation (12) from Pudritz et al. 2007), where R_0 is the minimum radius at which the magnetic field lines thread the disk. The escape velocity at R_0 is given by

$$v_{\rm esc} = \left(\frac{2GM}{R_0}\right)^{\frac{1}{2}}, \tag{9}$$

where M is the mass of the HSC. This assumes that the mass is dominated by the HSC. The central temperature of the HSC is given by

$$T_c = \alpha\left(\frac{\mu m_{\rm H}}{k}\right)\left(\frac{GM}{R}\right), \tag{10}$$

where R is the radius of the HSC. Assuming that $R_0 \approx 4R$, which is consistent with the inner disk radii inferred for young stellar objects, (e.g., Bouvier et al. 2007), we can write the central temperature of the HSC as

$$T_c \approx \alpha\left(\frac{2\mu m_{\rm H}}{k}\right)\left(\frac{R_0}{R_a} v_{\rm out}\right)^2. \tag{11}$$

In this equation, R_a is the launching radius of the outflow. To evaluate the equation, we assume a convective star (i.e., a $n = 1.5$ polytrope) where $\alpha = 0.54$, $m_{\rm H}$ is the mass of a hydrogen atom, and μ is the mean molecular weight, which is 2.4 for molecular gas and 1.33 for atomic gas. The ratio of R_0 to R_a is taken as one-third (Pudritz et al. 2007).

The maximum velocity of ~18 km s^{-1} for each outflow lobe in HOPS 400-A and HOPS 403 yields a central temperature of ~10,000 K, which is above the dissociation temperature of molecular hydrogen. The actual maximum velocities and resulting temperatures may be a factor of two higher, due to the inclination of the outflow. The short dynamical ages of the outflows support the idea that these are very young protostars that have evolved past the FHSC stage.

On the other hand, the maximum outflow velocity of HOPS 404 is ~2 km s^{-1} in both outflow lobes. This implies a central temperature of ~140 K, which is below the dissociation

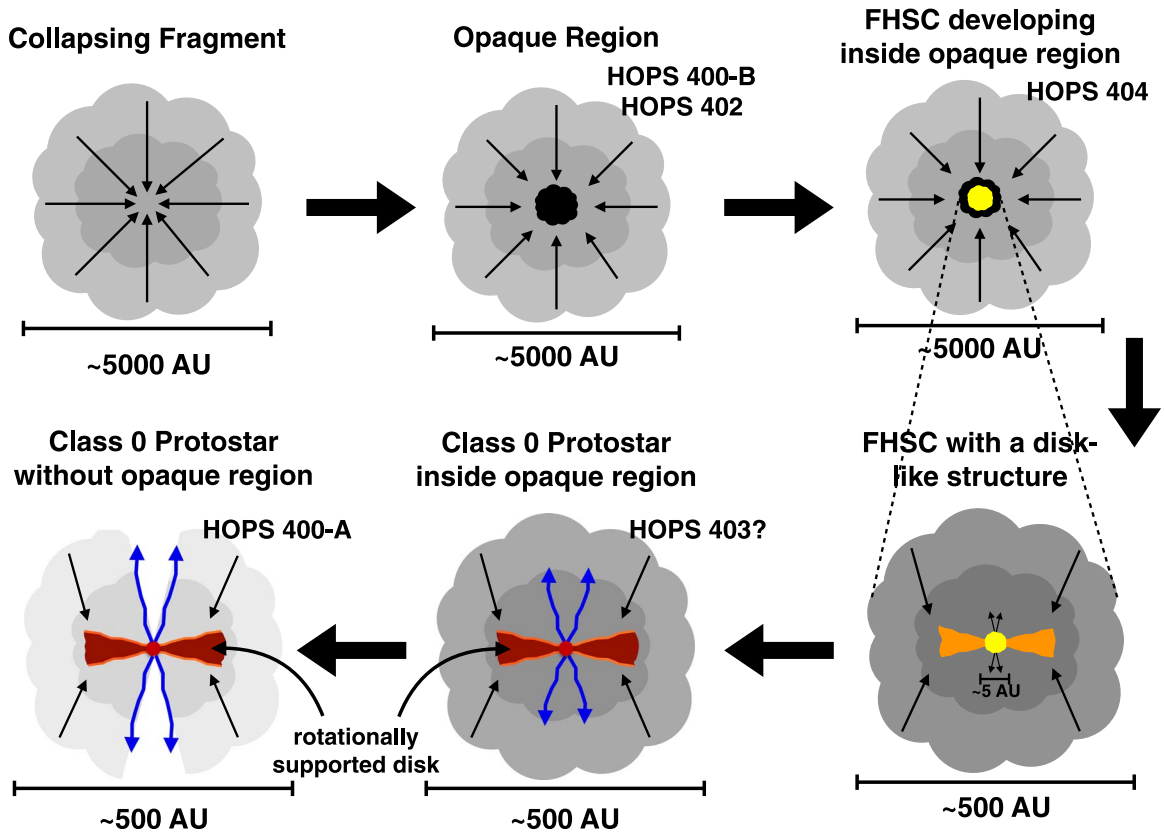

Figure 11. A cartoon schematic of the evolutionary sequence for the earliest phases of low-mass star formation, as suggested by our observations and as seen from an edge-on inclination with respect to the angular momentum or magnetic field axis. The upper left begins with a collapsing fragment of gas and dust. The upper middle continues with the formation of an opaque region at the center of the collapsing fragment with continuing gravitational infall. The upper right is an FHSC forming within the opaque region. The bottom right is an FHSC with a disk-like structure and an outflow beginning. The bottom middle depicts the formation of a Class 0 protostar inside the opaque region that may have a rotationally supported disk and more well-defined outflows. The final step depicted in the bottom left is of a typical Class 0 protostar with outflows that have broken through the envelope, an actively accreting, rotationally supported disk, and continued infall from the slowly dissipating envelope.

temperature of molecular hydrogen by more than an order of magnitude. Thus, the slow velocity suggests the outflow is driven by an FHSC. This FSHC would be unresolved and located within the extended dust emission that we observe.

The maximum velocities of 2 km s^{-1} are also consistent with model predictions of FHSC outflow velocities (Price et al. 2012). In comparison, Gerin et al. (2015) detect outflows associated with the Barnard 1b FHSC candidate with velocities up to ~7 km s^{-1} and estimated a dynamical age of ~1000 and ~2000 yr for B1b-S and B1b-N, respectively. They note that the outflow masses, mass-loss rate, and mechanical luminosities agree with theoretical predictions of FHSC.

The presence of HSCs in HOPS 400-B and HOPS 402 is less clear, and the data presented here cannot absolutely rule out outflows from either source. The 8 mm continuum image of HOPS 400-B demonstrates a compact emission peak off center from the overall emission that may mark the presence of a hydrostatic core. HOPS 402 lacks a clear compact emission peak in either wavelength, and the brightness temperature profiles are the broadest and coldest in this sample (Figure 3).

4.4. Evolutionary Context and Scenario for Irregular PBRs

Figure 11 is a cartoon schematic visualizing the formation of a low-mass star incorporating our interpretation of how the irregular PBRs fit into the broader context of star formation. The viewing angle is assumed to be edge-on with respect to the angular momentum axis. In the upper left, the first step is a collapsing fragment of gas and dust. An opaque region develops in the central region of the collapsing fragment, which is represented in the top middle. The top right represents an FHSC developing inside the opaque region with a disk-like structure forming. The bottom right shows the inner region, where a rotationally supported disk or disk-like structure has formed, as well as an outflow. The bottom middle is a Class 0 protostar inside an optically thick region that contains a rotationally supported disk and more well-defined outflows. Finally, depicted in the bottom left, the Class 0 protostar continues to evolve without an optically thick region. This phase has an outflow driven by a rotationally supported disk.

We interpret HOPS 402 as an opaque region that may not have an FHSC. HOPS 400-B may be more evolved than HOPS 402, due to the point-like peak at 8 mm, but still may not have an HSC. HOPS 403 may represent an intermediate phase where a Class 0 protostar is launching an outflow but it still has a large opaque region, if it is not a binary. The Perseus protostar IRAS 4A1 (scenario 2 of Sahu et al. 2019; Santangelo et al. 2015) may also be an example of this phase. HOPS 403 may be similar to IRAS 4A1 in that it has a large optically thick region and may be driving an outflow consistent with having

formed a second core. Alternatively, the HOPS 403 outflow may be driven by a companion. HOPS 404 is an FHSC candidate that has developed inside an optically thick region. The outflow detected implies a disk or disk-like structure within the opaque region. Once the central temperature of the FHSC reaches ~2000 K, it evolves into a Class 0 protostar with a rotationally supported disk and more well-defined outflows. HOPS 400-A appears to be a young Class 0 protostar with a small disk and more typical flux densities at 0.87 mm and 8 mm.

4.5. The Concentration of Irregular PBRs in Orion B

As noted by Stutz et al. (2013), 13 of the 19 PBRs are located in the Orion B cloud.[13] This concentration is even more extreme for the irregular PBRs, all of which are found in Orion B. In contrast, Orion B has 69 out of 330 protostars and 30 out of the 62 Class 0 protostars in the HOPS survey. The concentration of irregular PBRs in Orion B may be explained by environmental differences in Orion B, which has led to the formation of the irregular PBRs. In this case, $t_{\rm stat}$ would be significantly higher, as in our original calculation, we assumed the total number of protostars in Orion A and B. Alternatively, Orion B may be undergoing a rapid acceleration of its star formation rate (Fischer et al. 2017). Either of these proposed solutions has important implications for the star formation process, and future observations and modeling are needed to further understand the concentration of PBRs in Orion.

5. Summary

We present the detection of four extended, irregular structures resolved in ~0.″1 (40 au) resolution ALMA 0.87 mm and VLA 8 mm imaging that may represent the youngest protostars in Orion. These protostars are HOPS 400-B, 402, 403, and 404 (Furlan et al. 2016), and are part of a sample of very red, young protostars identified in *Herschel* observations of Orion (the PACS bright red sources or PBRs; Stutz et al. 2013).

The four irregular protostars are distinguished by high VLA flux densities compared to the remainder of the PBR sample and by their bright 0.87 mm emission that is optically thick over most of the observed structures. This emission extends out to radii of ~55–84 au (half maximum) and implies peak dust temperatures ranging from 41 to 170 K. Based on their average dust temperatures, the masses estimated from the 8 mm data range from 0.5 to 1.2 $M_\odot$ and depend strongly on the adopted opacities. These appear to be the center of collapsing cloud fragments that are optically thick to their own radiation.

There are three timescales associated with the opaque regions of these protostars: the freefall time ($t_{\rm ff}$), the Kelvin–Helmholtz time ($t_{\rm KH}$) or cooling time, and the statistical lifetime ($t_{\rm stat}$). The $t_{\rm ff}$ for the four irregular protostars are ~100 yr, whereas the $t_{\rm KH}$ determined with the observed luminosities range from 250 to 3600 yr. The masses used to calculate $t_{\rm KH}$ strongly depend on the adopted dust opacities. The value of $t_{\rm KH}$ can be equal to the $t_{\rm ff}$ for masses at the low end of the plausible range. However, because the irregular PBRs make up ~1.5% of the HOPS protostars, their statistical lifetime is 6000 yr if they represent a distinct phase in protostellar evolution, assuming a constant star formation rate. This is close to the higher values of $t_{\rm KH}$ obtained with our higher estimated masses and requires internal support against gravity to prevent collapse. Due to their consistency with $t_{\rm stat}$, we favor the longer times and higher masses.

Thermal pressure alone is insufficient to support the irregular PBRs from collapse, and alternative means of support are required. These include rotational support or a combination of magnetic, turbulent, and thermal support with the magnetic field dominating.

In the case of rotational support, the objects may be highly unstable disks, such as the prestellar disks predicted by simulations. The irregular structure and the lack of mid-IR emission or outflows expected for the face-on inclination implied by their morphologies make it unlikely that these are stable disks surrounding young protostars.

The compact outflows we detect in the ^{12}CO ($J = 3$–2) line indicate the presence of HSCs toward three sources with minimum ages set by the dynamical times of ~300–1400 yr. One of the sources is HOPS 400-A, a companion Class 0 protostar to the irregular HOPS 400-B. The other is located toward a peak of HOPS 403; this may be from a source within the opaque region or a companion behind it. Finally, the low-velocity outflow from HOPS 404 suggests that it contains an FHSC.

Future studies of these irregular PBRs should include polarimetry designed to resolve the magnetic field structure and molecular-line-width observations to measure turbulent and/or rotational motions of the inner envelopes. These will reveal whether magnetic fields, rotation, and/or turbulent motions are sufficient to support the opaque regions against collapse.

We wish to thank the anonymous referee for insightful comments and suggestions that improved the quality of this manuscript. The authors acknowledge Lee Hartmann for the useful discussions and many insightful comments. Support for Nicole Karnath was provided by the NSF through award SOSP AST-1519126 from the NRAO and by the NASA Origin of the Solar System program 13-OSS13-0094 (Megeath PI for both). This work made use of the SIMBAD database, the Vizier database, and the NASA Astrophysics Data System, funded by the National Aeronautics and Space Administration and the NSF.

A.S. acknowledges funding through Fondecyt regular (project code 1180350), "Concurso Proyectos Internacionales de Investigación" (project code PII20150171), and Chilean Centro de Excelencia en Astrofísica y Tecnologías Afines (CATA) BASAL grant AFB-170002.

J.J.T. acknowledges funding from the National Science Foundation AST-1814762.

Z.Y.L. is supported in part by NSF 1716259 and NASA 80NSSC18K1095.

G.A., M.O., and A.K.D.-R. acknowledge financial support from the State Agency for Research of the Spanish MCIU through the AYA2017-84390-C2-1-R grant (co-funded by FEDER) and through the "Center of Excellence Severo Ochoa" award for the Instituto de Astrofisica de Andalucia (SEV-2017-0709).

This research was conducted in part at the SOFIA Science Center, which is operated by the Universities Space Research

[13] One source previously identified as being in the Orion B cloud, HOPS 354, is found in the Lynds 1622 cloud. An analysis of *Gaia* DR2 parallaxes by Kounkel et al. (2018) indicates that this cloud is in the foreground of Orion B and is the same distance as the Orion OB1a association (345 ± 6 pc).

Association under contract NNA17BF53C with the National Aeronautics and Space Administration.

The National Radio Astronomy Observatory is a facility of the National Science Foundation operated under cooperative agreement by Associated Universities, Inc. This paper makes use of the following ALMA data: ADS/JAO.ALMA# 2015.1.00041.S. ALMA is a partnership of ESO (representing its member states), NSF (USA), and NINS (Japan), together with NRC (Canada), MOST and ASIAA (Taiwan), and KASI (Republic of Korea), in cooperation with the Republic of Chile. The Joint ALMA Observatory is operated by ESO, AUI/NRAO and NAOJ.

Software: CASA (McMullin et al. 2007).

Appendix

A.1. HOPS 400-A

HOPS 400-A is a Class 0 protostar driving an outflow and is more evolved than its extended companion, HOPS 400-B. It has 0.87 and 8 mm flux densities similar to other Class 0 protostars in the VANDAM Orion sample, is marginally resolved in the ALMA and VLA data, and is driving a strong outflow (Figures 2 and 4). Its millimeter emission likely arises from a marginally resolved disk (Tobin et al. 2020). We interpret this protostar as a second-stage HSC with a disk and outflow, similar to other Class 0 protostars in the VANDAM Orion sample. HOPS 400-A must have an unresolved temperature gradient and inner optically thick regions or disk. HOPS 400-A and -B are likely embedded in the same infalling, protostellar envelope. In the *Spitzer*, *Herschel*, and *APEX* data, they are not resolved and the resulting SED is a composite of the two (Furlan et al. 2016).

HOPS 400-A has a bent morphology in the outflow as seen in Figure 4. Assuming that this bent nature is due to the motion of the protostar through the surrounding envelope. We estimate a velocity of 2.6 km s^{-1} relative to its natal core. The value of the velocity adopts the average maximum velocity of the outflow from the red and blue lobes, half of the spatial distance in the *y*-direction, and the average *x*-direction distance of the blue and red lobes. It is unclear from this data whether the bent morphology originates from the proper motion of the binary or if it originates from the orbital motion of 400-A with respect to 400-B. The dynamical age of the outflow is ∼700 yr.

Another possibility is that HOPS 400-B has an outflow that is hidden near the large optically thick continuum resulting in a superposition of two outflows. If this is the case, the outflows cannot be distinguished by the data presented in this paper, and the outflow properties in Table 5 may be a combination of two outflows instead of one.

A.2. HOPS 400-B

The southern companion to HOPS 400-A extends almost 200 au in diameter, at both 0.87 and 8 mm, with a peak to the south. The peak is more evident in the 8 mm band and is offset from the geometric center of the mass distribution; this is contrary to the nominal expectation of a protostar forming at the center of its envelope or disk. The brightness temperature profiles in Figure 3 show a compact, central peak at 8 mm. This indicates the presence of a warm, compact density peak that is not apparent in the optically thick 0.87 mm emission. However, it is not clear whether or not HOPS 400-B contains an HSC. HOPS 400-B is different from typical isothermal starless/prestellar cores in that the compression of gas in the opaque region is generating a significant amount of luminosity due to the high density of the gas. It is also possible that HOPS 400-B is either blended with the HOPS 400-A outflow or contains an HSC and has launched an outflow that has not yet broken through the inner, dense envelope and therefore cannot be detected with the current ALMA data. Longer wavelength ALMA data may detect such an outflow in CO ($J = 1$–0) due to the lower opacity at 2.7 mm.

A.3. HOPS 401

HOPS 401 is located within 15,000 au of the irregular protostar HOPS 402, and like its neighbor, HOPS 401 has a very cold SED and lacks a detection at 24 μm (Stutz et al. 2013; Furlan et al. 2016). It is more compact than the irregular PBRs, spatially extended at 0.87 mm, barely resolved at 8 mm, and appears to be optically thick within the inner 29 au at 0.87 mm (Table 2). HOPS 401 either has a temperature gradient or an optical depth at 8 mm that approaches 1. The flux densities are similar to the rest of the PBR sample. Despite having 8 mm flux densities comparable to the typical PBRs, we include HOPS 401 in this analysis due to its cold SED, proximity to HOPS 402, and its hint of an irregular morphology.

There is high-velocity ^{12}CO emission near the source, although it is not clear from our ALMA snapshot data if this is from an outflow driven by the protostar, an outflow from another protostar, or motions in the surrounding cloud (Figure 5). The outflow lobes are not as distinct, are not exactly centered on the protostar, and have a bent morphology in the outflow similar to HOPS 400-A. If the bent nature is due to the motion of the protostar, the estimated velocity is ∼7.5 km s^{-1} relative to its natal core. The procedure to determine the velocity value is the same as for HOPS 400-A. The dynamical age of the outflow is ∼300 yr.

Unlike the other four protostars with resolved optically thick zones, the freefall time of HOPS 401 is consistent with the Kelvin–Helmholtz timescale due to its lower inferred mass. Although its spatially resolved morphology appears irregular and not disk-like, HOPS 401 is not as extended at 8 mm as the other four sources. We did not include it in our primary analysis for this reason, yet it likely traces a very early stage of protostellar evolution and perhaps represents a pathway for hydrostatic core formation that does not produce a large optically thick zone. If this is the case, then the required duration for the four irregular protostars is higher than the value of $t_{\rm stat}$ estimated in Section 4.1.

A.4. HOPS 402

HOPS 402 has an asymmetric structure at 0.87 and 8 mm extending 150 au at 0.87 mm. The 8 mm data has an elongated structure with a peak to the south and a triangular-shaped morphology coincident with the more extended 0.87 mm peak. The brightness cut in Figure 3 shows an extended and asymmetric structure with a compact 8 mm peak that is not visible at 0.87 mm. Here, the peak 0.87 mm continuum is brighter, but the temperatures become comparable at the peak, again the signature of high optical depth at 0.87 mm.

Similar to HOPS 400-B, it is not clear whether or not HOPS 402 contains an HSC. There is no compact peak at

either wavelength, but the compression of gas in the opaque region generates a significant amount of luminosity, due to the high density of the gas. Although the luminosities and T_{bol} are the lowest of the PBR sample, it is possible HOPS 402 contains an HSC. This HSC may have launched an outflow that has not broken through the high-opacity region and cannot be detected with the current ALMA data.

A.5. HOPS 403

HOPS 403 at 0.87 mm exhibits a roughly circular symmetry, extends over 150 au in diameter, and has an elongated peak to the southeast. It shows a point-like peak at 8 mm that is coincident with the more elongated, lower contrast 0.87 mm peak. HOPS 403 is asymmetric in both wavelength cuts (Figure 6) with the 0.87 mm peak offset from the 8 mm peak. The 8 mm peak has an almost point-like shape but widens out past ~40 au. The fact that the 8 mm brightness temperature at this peak is almost double the 0.87 mm brightness temperature again indicates a high optical depth in the submillimeter with the 0.87 mm tracing cooler dust. The 0.87 mm emission is flatter outside of ~50 au, but is still within a factor of two to the 8 mm brightness temperature. The 8 mm peak is thought to be the source of the outflow, which would be more evolved than an FHSC as inferred from the outflow velocities, although we cannot trace the outflow directly to the source, due to the high opacity at 0.87 mm. The dynamical age of the outflow is ~300 yr.

A second, fainter 8 mm peak not present in the 0.87 mm continuum supports that this source may be forming a binary. In this case, the bright 8 mm peak may be located inside the optically thick region, or it maybe located behind the region. In the latter case, this orientation would be similar to HOPS 400 if observed from an orientation where HOPS 400-A is behind 400-B. Both would be forming in the center of the same infalling envelope, and the observed SEDs from *Spitzer*, *Herschel*, and *APEX* would be a composite SED for this entire system (Furlan et al. 2016).

A.6. HOPS 404

HOPS 404 has a box-like morphology at 8 mm and is an FHSC candidate. Unlike the other three irregular PBRs, the 0.87 mm continuum is more circularly symmetric and at both wavelengths, the continuum is the most compact of the four irregular PBRs.

The outflow morphology of HOPS 404 also shows a bent, poorly collimated outflow, perhaps demonstrating a rotation or precession of the outflow, the latter being the case if the outflow is more aligned in the plane of the sky (inclination > 60°, Figure 7). This will reduce the measured radial velocity and consequently increase the resulting dynamical lifetime of the outflow to ~1400 yr, which is larger than the HOPS 400-A and HOPS 403 dynamical lifetimes (~500 yr). These lifetimes should be considered lower limits; the faster HOPS 400-A and HOPS 403 outflows may not have been fully mapped by ALMA. Thus, the HOPS 400-A and HOPS 403 HSCs can be older than the HOPS 404 FHSC.

ORCID iDs

N. Karnath https://orcid.org/0000-0003-3682-854X
S. T. Megeath https://orcid.org/0000-0001-7629-3573
J. J. Tobin https://orcid.org/0000-0002-6195-0152
A. Stutz https://orcid.org/0000-0003-2300-8200
P. Sheehan https://orcid.org/0000-0002-9209-8708
S. Sadavoy https://orcid.org/0000-0001-7474-6874
I. W. Stephens https://orcid.org/0000-0003-3017-4418
G. Anglada https://orcid.org/0000-0002-7506-5429
E. Cox https://orcid.org/0000-0002-5216-8062

References

Basu, S., & Mouschovias, T. C. 1994, ApJ, 432, 720
Bate, M. R. 1998, ApJL, 508, L95
Bate, M. R. 2011, MNRAS, 417, 2036
Bate, M. R., & Lorén-Aguilar, P. 2017, MNRAS, 465, 1089
Bate, M. R., Tricco, T. S., & Price, D. J. 2014, MNRAS, 437, 77
Bergin, E. A., & Tafalla, M. 2007, ARA&A, 45, 339
Bhandare, A., Kuiper, R., Henning, T., et al. 2018, A&A, 618, A95
Bouvier, J., Alencar, S. H. P., Harries, T. J., Johns-Krull, C. M., & Romanova, M. M. 2007, in Protostars and Planets V, ed. B. Reipurth, D. Jewitt, & K. Keil (Tucson, AZ: Univ. Arizona Press), 479
Commerçon, B., Audit, E., Chabrier, G., & Chièze, J.-P. 2011, A&A, 530, A13
Commerçon, B., Levrier, F., Maury, A. J., Henning, T., & Launhardt, R. 2012, A&A, 548, A39
Cox, E. G., Harris, R. J., Looney, L. W., et al. 2015, ApJL, 814, L28
Dall'Olio, D., Vlemmings, W. H. T., Persson, M. V., et al. 2019, arXiv:1905.00415
Dunham, M. M., Arce, H. G., Mardones, D., et al. 2014, ApJ, 783, 29
Fischer, W. J., Megeath, S. T., Furlan, E., et al. 2017, ApJ, 840, 69
Fischer, W. J., Megeath, S. T., Stutz, A. M., et al. 2013, AN, 334, 53
Furlan, E., Fischer, W. J., Ali, B., et al. 2016, ApJS, 224, 5
Gerin, M., Pety, J., Fuente, A., et al. 2015, A&A, 577, L2
Girart, J. M., Beltrán, M. T., Zhang, Q., Rao, R., & Estalella, R. 2009, Sci, 324, 1408
González Lobos, V., & Stutz, A. M. 2019, MNRAS, 489, 4771
Hartmann, L. 2009, Accretion Processes in Star Formation: Second Edition (Cambridge: Cambridge Univ. Press)
Heitsch, F. 2013, ApJ, 769, 115
Hernández-Gómez, A., Loinard, L., Chandler, C. J., et al. 2019, ApJ, 875, 94
Klessen, R. S., & Hennebelle, P. 2010, A&A, 520, A17
Kounkel, M., Covey, K., Suárez, G., et al. 2018, AJ, 156, 84
Kristensen, L. E., & Dunham, M. M. 2018, A&A, 618, A158
Larson, R. B. 1969, MNRAS, 145, 271
Low, C., & Lynden-Bell, D. 1976, MNRAS, 176, 367
Mac Low, M.-M., Klessen, R. S., Burkert, A., & Smith, M. D. 1998, PhRvL, 80, 2754
Masunaga, H., & Inutsuka, S.-I. 2000, ApJ, 531, 350
Masunaga, H., Miyama, S. M., & Inutsuka, S. I. 1998, ApJ, 495, 346
Mathis, J. S., Rumpl, W., & Nordsieck, K. H. 1977, ApJ, 217, 425
Matsumoto, T., & Hanawa, T. 2003, ApJ, 595, 913
McKee, C. F. 1999, in The Origin of Stars and Planetary Systems, ed. C. Series, C. J. Lada, & N. D. Kylafis (Dordrecht: Springer), 29
McMullin, J. P., Waters, B., Schiebel, D., Young, W., & Golap, K. 2007, ASP Conf. Ser. 376, Astronomical Data Analysis Software and Systems XVI, ed. R. A. Shaw, F. Hill, & D. J. Bell (San Francisco, CA: ASP), 127
Myers, P. C., Basu, S., & Auddy, S. 2018, ApJ, 868, 51
Offner, S. S. R., & Liu, Y. 2018, NatAs, 2, 896
Ormel, C. W., Min, M., Tielens, A. G. G. M., Dominik, C., & Paszun, D. 2011, A&A, 532, A43
Ossenkopf, V., & Henning, T. 1994, A&A, 291, 943
Price, D. J., Tricco, T. S., & Bate, M. R. 2012, MNRAS, 423, L45
Pudritz, R. E., Ouyed, R., Fendt, C., & Brandenburg, A. 2007, in Protostars and Planets V, ed. B. Reipurth, D. Jewitt, & K. Keil (Tucson, AZ: Univ. Arizona Press), 277
Rees, M. J. 1976, MNRAS, 176, 483
Sahu, D., Liu, S.-Y., Su, Y.-N., et al. 2019, ApJ, 872, 196
Saigo, K., Matsumoto, T., & Hanawa, T. 2000, ApJ, 531, 971
Saigo, K., Tomisaka, K., & Matsumoto, T. 2008, ApJ, 674, 997
Santangelo, G., Codella, C., Cabrit, S., et al. 2015, A&A, 584, A126
Schneider, N., André, P., Könyves, V., et al. 2013, ApJL, 766, L17
Segura-Cox, D. M., Harris, R. J., Tobin, J. J., et al. 2016, ApJL, 817, L14
Silk, J. 1977, ApJ, 214, 152
Stutz, A. M., & Gould, A. 2016, A&A, 590, A2
Stutz, A. M., Tobin, J. J., Stanke, T., et al. 2013, ApJ, 767, 36
Tychoniec, Ł., Tobin, J. J., Karska, A., et al. 2018, ApJ, 852, 18

Tobin, J. J., Sheehan, P., Megeath, S. T., et al. 2020, ApJ, 890, 130
Tobin, J. J., Stutz, A. M., Manoj, P., et al. 2016, ApJ, 831, 36
Tobin, J. J., Stutz, A. M., Megeath, S. T., et al. 2015, ApJ, 798, 128
Tomisaka, K. 2002, ApJ, 575, 306
Tsuribe, T., & Inutsuka, S.-I. 1999a, ApJ, 526, 307
Tsuribe, T., & Inutsuka, S.-I. 1999b, ApJL, 523, L155
van der Marel, N., Kristensen, L. E., Visser, R., et al. 2013, A&A, 556, A76
Vaytet, N., Chabrier, G., Audit, E., et al. 2013, A&A, 557, A90
Woitke, P., Min, M., Pinte, C., et al. 2016, A&A, 586, A103
Yıldız, U. A., Kristensen, L. E., van Dishoeck, E. F., et al. 2015, A&A, 576, A109